Improved radiative transfer corrections in helium emission lines

Oleg Kurichin * and Alexandre Ivanchik
Ioffe Institute, Polytechnicheskaya 26, 194021 Saint Petersburg, Russia

(Received 25 September 2025; accepted 14 January 2026; published 6 February 2026)

We present a new detailed model of the He I collisional-recombination spectrum based on the most up-to-date atomic data. The model accounts for radiative transfer effects and the influence of a nonzero optical depth in He I lines arising from transitions to the metastable 2^3S state. The model reveals substantial deviations in the emissivities of the λ3889 and λ7065 lines in case of a nonzero optical depth, with previous models systematically underestimating and overestimating them by 5% to 20%, respectively. In the optically thin case, however, our results show good agreement with previous studies. Using the new model, we compute optically thin emissivities for a wide set of UV, optical, and IR He I recombination lines over a fine grid of electron densities and temperatures which are typical for H II regions and planetary nebulae ($1 \leq n_e \leq 10^4$ cm^{-3}, $8000 \leq T_e \leq 22000$ K). In addition, we present new fitting formulas for radiative transfer corrections for several He I lines relevant to optical and near-IR observations, covering $0 \leq \tau_{3889} \leq 10$ within the same density and temperature ranges. The accuracy of the obtained approximations is $\lesssim$0.1% within the specified parameter range. These results can be readily implemented in modern codes for determining the primordial ^{4}He abundance and are also applicable to a broader range of spectroscopic analyses of He I emission lines.

DOI: 10.1103/rf57-k9yj

I. INTRODUCTION

Analysis of helium emission lines is a powerful diagnostic tool for probing the physical conditions and chemical composition of a various astrophysical objects. In particular, modeling the emission spectra of low-metallicity blue compact dwarf galaxies has become the most reliable method for obtaining independent estimates of the abundance of primordial helium, Y_p. The combination of high-quality spectroscopic data and advanced photoionization models that take into account various systematic effects has made it possible to determine Y_p with remarkable accuracy ($\lesssim$1.5%) [1–12]. Consequently, one of the major directions of studies is the improvement of methods for quantifying and correcting for systematic uncertainties in photoionization models.

Among the most important sources of systematic uncertainty are the theoretical emissivities of He I lines and the treatment of radiative transfer effects. For many of the strongest transitions associated with the metastable 2^3S level of He I, the optical depth is non-negligible. For example, observational estimates of optical depth in the He I λ3889 line (it corresponds to transition $3^3P \to 2^3S$ and is one of the strongest He I emission lines in the optical range) fall in the range $0 \lesssim \tau_{3889} \lesssim 5$ [2,8,9]. The presence of a nonzero optical depth leads to the attenuation of some lines and the enhancement of others. Typically, line fluxes vary within ~1%–5%, but for some lines (like, e.g., λ3889 or λ7065) changes can reach values of ~30% at certain values of optical depth [13]. If these effects are not properly accounted for, they can introduce systematic shifts in the derived helium abundances, and consequently bias the estimates of Y_p.

The nonzero optical depth in some helium lines appears for the following reason. Unlike hydrogen, helium has two separate transition ladders: singlet ladder with total spin of electrons $S = 0$ and triplet ladder with $S = 1$. The transition from the first exited state 2^3S in triplet ladder to the ground state 1^1S (which is singlet) is strongly forbidden with $A = 1.27 \times 10^{-4}$ sec^{-1} [14], making the 2^3S level metastable. As a result, photons emitted from $n^3P \to 2^3S$ radiative transitions can be efficiently reabsorbed, significantly altering the populations of the affected levels. Through collisional mixing, these changes propagate to many other levels, ultimately leading to substantial deviations in the observed fluxes of several He I lines. To account for this effect, a so-called optical depth function, f_τ, is included in photoionization models. The optical depth function is defined as the ratio between the emissivity calculated at a given optical depth τ and the emissivity in the optically thin case (e.g., Ref. [13]), as follows:

$$f_\tau(\lambda, n_e, T) = \frac{E_\lambda(\tau \neq 0, n_e, T)}{E_\lambda(\tau = 0, n_e, T)}. \tag{1}$$

*Contact author: o.chinkuir@gmail.com

In modern photoionization models used for primordial helium studies, f_τ is implemented as a multiplicative correction factor (see, e.g., Refs. [2,6,8,9]). All modern models adopt the analytic function proposed in Ref. [13]:

$$f_\tau(\lambda, n_e, T) = 1 + \frac{\tau}{2}\left(a_\lambda + \frac{T}{10^4\ \mathrm{K}} \times \sum_{i=0}^{2} b_\lambda^{(i)} n_e^i\right), \quad (2)$$

where τ is the optical depth in the $\lambda3889$ line, and $a_\lambda, b_\lambda^{(i)}$ are fitting coefficients. Radiative transfer corrections for different lines are calculated using optical depths normalized to optical depth of this $\lambda3889$ line [15].

Despite the wide use of function (2), it suffers from several limitations:

(i) Function (2) assumes a linear dependence on τ, which does not always hold for different transitions. For example, emissivity of the $\lambda7065$ line corresponding to $3^3S \to 2^3P$ transition shows strong nonlinear dependence on τ (see Ref. [13]), which is not accounted for in function (2).

(ii) The formal applicability range of function (2) set in Ref. [13] is limited to $1 \le n_e \le 300\ \mathrm{cm}^{-3}$, $12000 \le T \le 20000$ K, and $\tau \le 2$. These constraints may be incompatible with the actual physical conditions in low-metallicity dwarf galaxies. For example, the object SBS $1135 + 581$ studied in Ref. [2] has the estimated temperature of $T = 11226 \pm 550$ K, and the object SBS 0335-052 has $T = 21780 \pm 3360$ K. Objects J0519 + 0007 and SBS 1152 + 579 from the same paper have estimated electron densities of $675 \pm 143\ \mathrm{cm}^{-3}$ and $452 \pm 197\ \mathrm{cm}^{-3}$, respectively. Objects SBS 0335–052, J0519 + 0007, and Mrk 450 all have estimated optical depth $\tau > 2$. These examples clearly demonstrate that the physical conditions in real galaxies may lie outside the applicability range of function (2). Therefore, its usage “as it is” for analysis of a large set of different galaxies with different physical conditions may introduce a systematic bias into the results.

(iii) Function (2) was obtained as a fit of emissivities computed with the simplified models of He I recombination spectrum of Refs. [13,16], which rely on atomic data, largely computed in the late 1980s and early 1990s. The models are based on radiative data and recombination cascades from Refs. [17,18], combined with collisional data from Ref. [19]. The only difference between the models of Refs. [16,13] is the number of modeled levels: $n_{\max} = 5$ for Ref. [16] and $n_{\max} = 20$ for Ref. [13]. In contrast, modern models of He I emission make use of much more accurate atomic data for all relevant processes and explicitly include a substantially larger number of LS-resolved levels. For instance, the model of Ref. [20], which underlies essentially all recent studies of primordial helium, treats levels up to $n_{\max} = 100$ and includes an additional “top-off” pseudolevel to account for recombination into $n > 100$ levels. Similarly, the recent model of Ref. [21] resolves LS-levels up to $n = 40$ and adds n-resolved levels on top up to $n = 100$. Detailed comparisons of the impact of updated atomic data on theoretical emissivities were carried out in Refs. [20–22], demonstrating systematic discrepancies of order $\sim 1\% - 2\%$ between modern and older results for all key emission lines.

The listed shortcomings of the method from Ref. [13] for correction for radiative transfer in helium lines come from its internal properties. However, there is also an external problem with this method, related to its use in modern analysis. The direct use of function (2) in its current form may lead to uncontrollable systematic shifts in helium abundance estimates. The reason for that is the unintentional mixing of different atomic data when modeling the observed fluxes of helium lines. In modern photoionization codes, the helium-to-Hβ line flux ratio is defined via the equation

$$\frac{F(\lambda)}{F(\mathrm{H}\beta)} = y^+ \times \frac{E(\lambda, n_e, T)}{E(\mathrm{H}\beta, n_e, T)} \times f_\tau(\lambda, n_e, T) \times [\ldots]. \quad (3)$$

Here, F is the line flux (helium or Hβ), y^+ is the helium-to-hydrogen density ratio, E is the theoretical emissivity at given electron density n_e and temperature T, and f_τ is the optical depth function. The square bracket $[\ldots]$ denotes additional well-known systematic corrections such as corrections for underlying stellar absorption, interstellar reddening, etc. (a detailed discussion can be found in, e.g., Ref. [8]).

Ideally, the product $E(\lambda, n_e, T) \times f_\tau(\lambda, n_e, T)$ should represent the emissivity of line λ at the chosen optical depth τ, provided that both terms are derived from the same model of the He I spectrum. In practice, however, $E(\lambda, n_e, T)$ is calculated using the emission model based on modern atomic data [20,23], while f_τ relies on an outdated one [16]. The systematic biases introduced by combining emissivities from inconsistent spectrum models have never been quantitatively assessed.

In the absence of a better alternative, function (2) remains the universal choice in current primordial helium studies. The only recent attempt to overcome its restrictions is presented in Ref. [24], where the authors used the original code of Ref. [13] to compute f_τ over a much broader three-dimensional grid: $\log(n_e/\mathrm{cm}^{-3}) = 0$–6 in 0.25 dex steps, $T = 5000$–20000 K in 500 K steps, and $\tau_{3889} = 0$–15 in steps of 1. Interpolation across this grid provides values of f_τ beyond the original fitting range. While this approach extends the practical use of the function (2), it does not address the more fundamental issue of the model of Ref. [13]—the reliance on outdated atomic data.

This study is aimed at developing a new model of the He I recombination spectrum based on the most up-to-date atomic data. Our primary goal is to construct this model and compute a refined grid of emissivities tailored to primordial helium studies. Equally important, we calculate a new optical depth function that resolves the shortcomings of the currently adopted prescription and, for the first time, ensures full consistency with the new set of helium emissivities. The key studies with which we compare our results are Refs. [16,20,21]. For the optical depth function, we compare our results with Ref. [13].

The collisional-recombination model of He I emissivities presented in this paper represents a global overhaul of the framework by Refs. [13,16], in which all relevant atomic data have been replaced with modern values and the number of modeled levels has been extended up to $n_{\max} = 50$. The key distinction of our model compared to more recent models of Refs. [20,21] lies in the treatment of collisional transitions between the low-lying excited states. In Refs. [20,21], the corresponding rates were obtained by linear interpolation over temperature grids of average collision strengths from Refs. [19,25] for transitions between levels with $n \leq 4$. In our model, the average collision strengths are instead calculated through direct integration of the high-resolution collision strengths data at a given temperature for transitions between levels with $n \leq 5$. Furthermore, we take into account the temperature dependence of the scaling factor used to calculate recombination rates onto Rydberg states with $l \leq 2$, which has not been considered previously. Altogether, our new model provides a more consistent and accurate description of the He I recombination spectrum, offering a solid foundation for future studies.

The structure of this paper is as follows: Sec. II is devoted to the atomic data employed in our emissivity model. Section III describes the construction of the model itself. In Sec. IV, we present the results of our emissivity calculations, provide an updated optical depth function, and compare our findings with those of the previous studies. Finally, our conclusions are summarized in Sec. V.

II. ATOMIC DATA

We use the following atomic data to construct collisional-recombination model of helium emissivities:

(1) Energy of LS-resolved sublevels E_k
(2) Einstein coefficients for transitions between sublevels A_{ik}
(3) Radiative recombination rates α_k
(4) Collision (de-)excitation rates q_{ik} and
(5) Rates of collisional ionization $C_k^{(ion)}$.

The main problem with the data is that for highly excited LS-resolved states in helium, no direct atomic data are available. In the subsections below, we provide all necessary information on how different atomic data are handled.

In the model, we consider only single electron transitions between excited levels with the second electron remaining in the ground state. Hereafter, we will use the following notation: by "level," we mean the set of all sublevels with the same value of the principal quantum number n, and "sublevel" or "state" stands for an LS-resolved state within a level. Throughout the paper, we characterize an excited sublevel via the notation $\gamma_k = [n_k, l_k, s_k]$, where n_k is the principal quantum number, l_k is the azimuthal quantum number, and $s_k = 2S_k + 1$ is the multiplicity of the sublevel k, which for helium can be either 1 for singlet ladder or 3 for triplet ladder. Also we use notation γ_u and γ_l or just indices u and l to distinguish upper and lower sublevels in a transition respectively. The values of all fundamental constants used throughout this paper are taken from the Particle Data Group (PDG) 2024 review [26].

A. Energy levels

The extensive table of energies for LS-resolved sublevels in the helium atom for $n \leq 10$ and $l \leq 7$ for both multiplicity ladders are presented in Ref. [27]. We use these essentially exact values for lower-lying excited sublevels. For sublevels with $n > 10$ and/or $l > 7$, we calculate energies from the Ritz quantum defect expansion as described in Ref. [28]. Energies of Rydberg states are expressed via the equation

$$E_k = \frac{R_M}{\nu^2} + \Delta E_k. \tag{4}$$

Here, R_M is the mass-corrected Rydberg constant, ν is the effective quantum number of a sublevel, and the term ΔE_k is used to account for relativistic and mass polarization corrections in helium. The explicit form of the latter is given via Eq. (11.54) in Ref. [28]. The effective quantum number of a sublevel is calculated by iterative solution of the equation

$$\nu = n - \delta(\nu). \tag{5}$$

Here, $\delta(\nu)$ is the quantum defect defined by Ritz expansion [28,29], as follows:

$$\delta(\nu) = \delta_0 + \frac{\delta_2}{(n-\delta)^2} + \frac{\delta_4}{(n-\delta)^4} + \dots. \tag{6}$$

Coefficients δ_i are constant values for a specified quantum numbers of l and s. For our model, we use coefficients from Table 11.9 in Ref. [28]. A detailed discussion of how these coefficients are calculated and why such expansion is applicable to Rydberg states in helium atoms can be found in Ref. [29]. It should be noted, that in this paper, we use data from the 2006 edition of Springer's *Handbook of*

Atomic, Molecular, and Optical Physics [28], while there are different editions from 1996, 2006, and 2023. One can use any of these books, since all data tables and accompanying formulas and explanations are the same throughout all editions, with the only difference being the number of the chapter.

B. A-values

Einstein coefficients A_{ul} for allowed radiative transitions between excited states in helium atoms are taken from Ref. [27]. As with the energy levels, in Ref. [27] only transitions between sublevels with $n \leq 10$ and $l \leq 7$ are considered. A-values for transitions involving sublevels with $n > 10$ and/or $l > 7$ are handled via one of the following methods.

If a transition $\gamma_u \to \gamma_l$ occurs between sublevels with $\gamma_u = [n_u > 10, l_u \leq 7, s_u]$ and $\gamma_l = [n_l \leq 7, l_l \leq 6, s_l]$ we calculate emission oscillator strength use extrapolation of data from Ref. [27] using the series suggested in Ref. [30]:

$$\ln(\nu_u^3 f_{ul}) = a + bx + cx^2. \tag{7}$$

Here, ν_u is effective quantum number of the upper sublevel, $x = \ln(E_l/\Delta E_{ul})$, $\Delta E_{ul} = E_u - E_l$. Effective quantum number and energies are calculated using the method described in Sec. II A. Fit parameters a, b, c are calculated using a trust region reflective algorithm based on data from Ref. [27]. Fit accuracy is better than 0.1% for the majority of transitions under consideration. An example of such extrapolation for the $n^1F \to 4^1D$ transition is presented in Fig. 1. The values of fitting coefficients for all transitions under consideration are presented in Appendix A.

If a transition $\gamma_u \to \gamma_l$ occurs between sublevels with $\gamma_u = [n_u > 10, l_u \leq 7, s_u]$ and $\gamma_l = [n_l > 10, l_l \leq 7, s_l]$, emission oscillator strengths are calculated using the Coulomb approximation. Coulomb approximation is a reliable and simple method to calculate transition probabilities in multielectron atomic systems. It was first proposed in Ref. [31]. The method assumes that the initial and final states of the atom differ primarily in the wave function of the transiting electron, which is approximated by a Coulomb wave function with correct asymptotic behavior at large radii. In multielectron atoms, wave functions of initial and final states are often expressed in terms of Whittaker functions, which are then integrated to obtain transition probability. In-depth review and discussion of the Coulomb approximation method can be found in, e.g., Ref. [32].

In this paper, we calculate oscillator strength for a transition $\gamma_u \to \gamma_l$ via the equation

$$f_{ul} = \frac{1}{(2L_l+1)(2S_u+1)} \sum_{J_u,J_l} (2J_l+1) \frac{\Delta\tilde{E}_{ul}}{|E_{J_u} - E_{J_l}|} f_{J_uJ_l}. \tag{8}$$

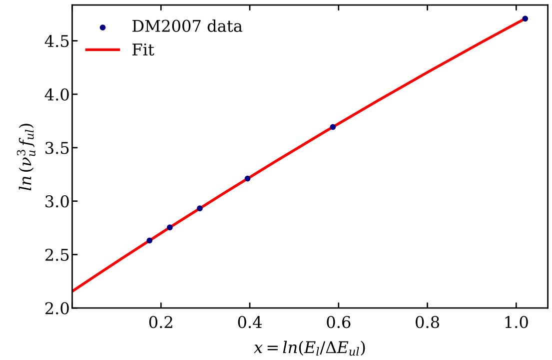

FIG. 1. Extrapolation of oscillator strength data from Ref. [27] (DM2007) using $n^1F \to 4^1D$ transition as an example. Lower values of x correspond to higher excited states.

Here, the summation is carried over all possible total angular momenta within a multiplet with energy weights, where $\Delta\tilde{E}_{ul}$ represents average transition energy. The oscillator strength for the individual members of the multiplet is obtained from the corresponding line strength $S(J_u, J_l)$, as follows:

$$f_{J_uJ_l} = \frac{1}{3(2J_l+1)} \frac{|E_{J_u} - E_{J_l}|}{hcR_M} \frac{S(J_u, J_l)}{a^2e^2}. \tag{9}$$

Here, $a = a_0(m_e/m_{He} + 1)$ is the scaled Bohr radius. Line strength is defined via the equation [32]

$$S^{1/2}(J_u,J_l) = (-1)^{\phi} \delta_{\kappa_u\kappa_l} \delta_{S_uS_l} [J_u,J_l,L_u,L_l]^{1/2} \times \begin{Bmatrix} L_u & J_u & S_u \\ J_l & L_l & 1 \end{Bmatrix} \begin{Bmatrix} l_u & L_u & L_1 \\ L_l & l_l & 1 \end{Bmatrix} P_{l_ul_l}. \tag{10}$$

Here, quantum numbers in upper case represent total quantum numbers of multielectron system, while those in lower case represent quantum numbers of initial and final states of transiting electrons. L_1 represents the total azimuthal quantum number of all electrons without the transiting one. Phase factor is $\phi = S_u + L_1 + J_l + l_l$. In Eq. (10), κ represents the remaining electron configuration of the atom without the transiting electron. Kronecker δ symbols are here to ensure that spin and electron configuration remain unchanged during the transition. Other quantities in Eq. (10) are defined via the following equations:

$$[J_u, J_l, L_u, L_l] = (2J_u+1)(2J_l+1)(2L_u+1)(2L_l+1). \tag{11}$$

Quantity $P_{l_ul_l}$ represents transition probability, as follows:

$$P_{l_ul_l} = -e(-1)^{l_u+l_>} \delta_{l_l,l_u\pm1} \sqrt{l_>} R_{n_ul_u,n_ll_l}. \tag{12}$$

Here, $l_> = \max(l_u, l_l)$. Kronecker δ ensures that the transition is dipole allowed. Value $R_{n_ul_u,n_ll_l}$ is the radial integral for an electric dipole transition. In this paper, we use $R_{n_u l_u, n_l l_l}$ as given in Ref. [33]:

$$R_{n_u l_u,n_l l_l} = \frac{a_0}{Z} K_u K_l \left(\frac{\nu_u \nu_l}{\nu_u+\nu_l}\right)^{\nu_u+\nu_l+2} \times \frac{\Gamma(\nu_u - l_l + 2)\Gamma(\nu_u + l_l + 3)}{\Gamma(\nu_u - \nu_l + 3)} \times \sum_{q=0}^{q_{\max}} a_q\, {}_2F_1(-\nu_l - l_l + 1, -\nu_l - l_l, \nu_u - \nu_l + 3 - q; y). \tag{13}$$

Here, a_0 is the Bohr radius, Z is the electric charge, Γ is the gamma function, and ${}_2F_1$ is the Gaussian hypergeometric function. Hartree's generalized normalization factors K_i are taken the same as in Refs. [31,33,34] and defined via the equation

$$K_i = \left(\frac{2}{\nu_i}\right)^{\nu_i} \frac{1}{\sqrt{\nu_i^2 \Gamma(\nu_i + l_i + 1)\Gamma(\nu_i - l_i)}}. \tag{14}$$

The hypergeometric function in Eq. (13) depends on parameter $y = (\nu_u - \nu_l)/(2\nu_u)$. Series coefficients a_q are calculated recursively starting from $a_0 = 1$ using the relation taken from Ref. [32], as follows:

$$a_q = \frac{\nu_l - \nu_u - 3 - q}{q} \frac{\nu_u + \nu_l}{2\nu_l} \times \frac{l_u(l_u+1) - (\nu_u - q)(\nu_u - q + 1)}{l_l(l_l+1) - (\nu_u - q + 2)(\nu_u - q + 3)} a_{q-1}. \tag{15}$$

Summation in Eq. (13) is truncated at $q_{\max} = \mathrm{round}(\nu_u - l_l + 1)$. The physical reasoning behind such criteria for truncation can be found in Ref. [32].

We sum Eq. (8) over total angular momenta J_u and J_l to obtain total multiplet oscillator strength. Summation over J can be easily done using the equality from Ref. [35], as follows:

$$\sum_{J_u, J_l} (2J_u + 1)(2J_l + 1) \begin{Bmatrix} L_u & J_u & S_u \\ J_l & L_l & 1 \end{Bmatrix}^2 = 2S_u + 1. \tag{16}$$

Thus, we obtain the following equation for oscillator strength averaged over multiplet:

$$f_{ul} = \frac{1}{3} \frac{\Delta E_{ul}}{hcR_M} \frac{l_>(2L_u+1)}{a^2} \begin{Bmatrix} l_u & L_u & L_1 \\ L_l & L_l & 1 \end{Bmatrix}^2 R^2_{n_u l_u, n_l l_l}. \tag{17}$$

The remaining Wigner $6j$-symbol can be easily calculated analytically, since we are modeling transitions in a two-electron helium atom. This means that the remaining electron is in the ground state; therefore, total azimuthal momentum is defined solely by the momentum of the transiting electron: $L_u = l_u$ and $L_l = l_l$, and also $L_1 = 0$. For the electric dipole transition, we have $l_l = l_u \pm 1$, and using exact formulas for Wigner $6j$-symbols from Ref. [36], we obtain the following expressions for them:

$$\begin{Bmatrix} l_u & l_u & 0 \\ l_l & l_l & 1 \end{Bmatrix} = \frac{(-1)^{2l_u}}{2} \sqrt{\frac{(2l_u+2)^2}{(l_u+1)(2l_u+1)(2l_u+3)}}, \tag{18}$$

$$\begin{Bmatrix} l_u & l_u & 0 \\ l_l & l_l & 1 \end{Bmatrix} = \frac{(-1)^{2l_u}}{2} \sqrt{\frac{4}{(2l_u-1)(2l_u+1)}}. \tag{19}$$

Equation (18) is for the case $l_l = l_u + 1$, and Eq. (19) is for $l_l = l_u - 1$.

The resulting form of oscillator strength for electric dipole transitions in Coulomb approximation in helium atoms is defined via the equation

$$f_{ul} = \frac{1}{3} \frac{\Delta E_{ul}}{hcR_M} \frac{l_>(2l_u+1)}{a^2} W^2_{6j} R^2_{n_u l_u, n_l l_l}. \tag{20}$$

Here, a is again the scaled Bohr radius, W_{6j} is defined via Eqs. (18) and (19), and the radial integral is defined via Eq. (13).

We calculate A-value from oscillator strength obtained via either of methods using Eq. (6.20) from Ref. [37], as follows:

$$A_{ul} = \frac{0.6670\ \mathrm{cm}^2\ \mathrm{s}^{-1}}{\lambda^2_{ul}} \frac{g_l}{g_u} f_{ul}. \tag{21}$$

Here, λ_{ul} is the wavelength of the emitted photon in centimeters, and g_i is the statistical weight of the i sublevel.

If a transition $\gamma_u \to \gamma_l$ occurs between sublevels with both $l_u > 7$ and $l_l > 7$, then A-values are calculated using hydrogenic approximation, since sublevels with $l > 7$ are essentially degenerate. The main difference from pure hydrogen transitions comes from the different mass of the helium atom and its electric charge. We calculate A-values using the algorithm described in Ref. [38]. In the paper, the authors present a fast and efficient iterative scheme for evaluation of hydrogenic line strength for arbitrary values of n and l. We created a Python 3 program based on this scheme to calculate hydrogenic A-values.

The general algorithm for evaluation of A-values is summarized in the flowchart presented in Fig. 2.

In the calculation, we use Case B approximation and thus set all A-values for transitions $n^1P \to 1^1S$ to zero. On top of A-values of the allowed transitions described above, we add some important A-values for forbidden transitions between lower-lying excited states. They include two-photon decay $2^1S \to 1^1S$ with $A = 50.94\,\mathrm{s}^{-1}$ from Ref. [39], forbidden transition $2^3S \to 1^1S$ with $A = 1.27 \times 10^{-4}\,\mathrm{s}^{-1}$ from Ref. [14], and forbidden transition $2^3P \to 1^1S$ with $A = 177.6\,\mathrm{s}^{-1}$ from Ref. [27].

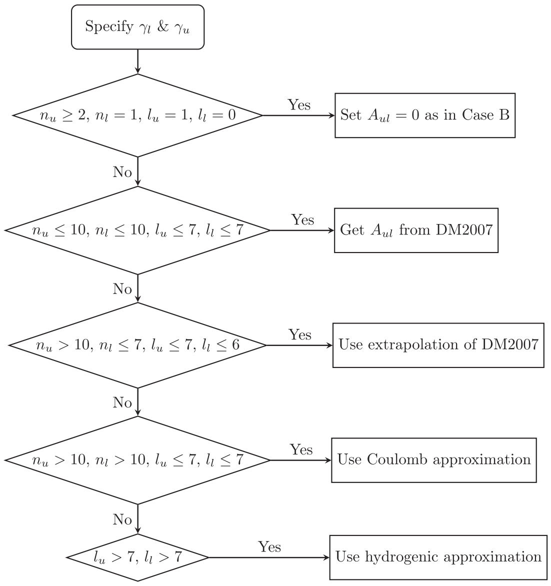

FIG. 2. Flowchart describing the algorithm for calculation of A-values for dipole-allowed transitions in helium atoms. DM2007 corresponds to Ref. [27].

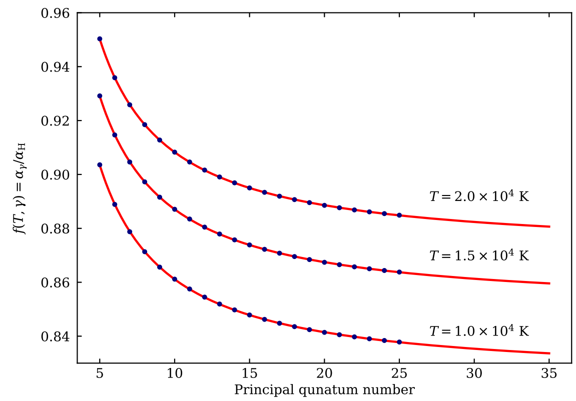

FIG. 3. Scaling factor $f(T,\gamma)$ for calculation of radiative recombination rate to levels n^1P for $T = 10^4$, 1.5×10^4, and 2×10^4 K. Blue circles represent exact data on ratio α_γ/α_H. Red line represents fit defined in Eq. (B2).

C. Radiative recombination rates

Radiative recombination rates for LS-resolved sublevels in He I are calculated using Eq. (14.2) from Ref. [37], as follows:

$$\alpha_\gamma(T) = \sqrt{\frac{8kT}{\pi m_e}} \int_0^\infty \sigma_{rr,\gamma}(E) \frac{E}{kT} \exp\left(-\frac{E}{kT}\right) d\frac{E}{kT}. \quad (22)$$

Here, T is temperature in K, and $\sigma_{rr,\gamma}(E)$ is the radiative recombination cross section to sublevel γ.

We calculate radiative recombination rates to sublevels with $n \leq 25$ and $l \leq 4$ using a direct integration of a large modern set of recombination cross sections from Ref. [30]. It should be noted that in Ref. [30], the authors present a set of photoionization cross sections. We obtain recombination cross sections from these data using the Milne relation.

We calculate radiative recombination rates to levels with $n > 25$ and/or $l > 4$ via the following methods. As noted in Ref. [30], there is a relation between He recombination rates and pure hydrogenic recombination rates for sublevels with $l \geq 4$, as follows:

$$\alpha_\gamma(T) = \frac{s}{4} \times \alpha_H(T, n, l). \quad (23)$$

Here, s is multiplicity of a sublevel, and $\alpha_H(T, n, l)$ is the pure hydrogenic recombination rate calculated for sublevels with the specified values of n, l. We use this relation to calculate radiative recombination rates to all levels with $l \geq 4$. We calculate hydrogenic recombination rates using Eq. (22), where the radiative recombination cross section is computed using the algorithm described in Ref. [38] (similar to one used for evaluation of hydrogenic A-values).

For levels with $n > 25$ and $l \leq 2$, we use a generalization of Eq. (23), as follows:

$$\alpha_\gamma(T) = f(T, \gamma) \times \alpha_H(T, n). \quad (24)$$

Here, $f(T, \gamma)$ is a scaling term defined via the following equation:

$$f(T, \gamma) = \frac{a_1(T)}{n^{a_2(T)}} + a_3(T). \quad (25)$$

Here, $a_i(T)$ are fit coefficients. Their dependence on temperature is determined by a fourth-degree polynomial with temperature T in K, as follows:

$$a_i(T) = \sum_{j=0}^{4} b_j^{(i)} \left(\frac{T}{10^4\ \mathrm{K}}\right)^j. \quad (26)$$

Fit parameters $b_j^{(i)}$ are calculated using a trust region reflective algorithm based on data from Ref. [30]. Accuracy of the fit is better than 1% for $5000 \leq T \leq 25000$ K. An example of such a fit for radiative recombination rates to levels n^1P for different temperatures is presented in Fig. 3. Fitting coefficients for the scaling term are presented in Appendix B.

D. Collisional transition rates

Calculation of collisional rates for transitions $\gamma_i \to \gamma_j$ is one of the most challenging aspects of the model, both computationally and physically, and must be approached with great care. Several types of collisional transitions can occur, and for some of them, direct and accurate atomic data are lacking. In such cases, one must rely on approximate methods of varying accuracy. Under the physical conditions typical of the interstellar medium in H II regions, the uncertainties introduced by these approximations are expected to be small, since the electron densities in such environments are relatively low (~10–1000 cm^{-3}). Nevertheless, this does not imply that collisional transitions can be neglected, as they have a substantial impact on many important optical and near-IR He I lines (e.g., $\lambda 7065$ and $\lambda 10830$). The influence of including collisional transitions on the resulting He I line emissivities can be assessed by comparing the models of He I spectrum from Refs. [40,22]. The former is a pure radiative-recombination model in which collisions are not included, whereas the latter is a full collisional-recombination model. In the collisionless model of Ref. [40], the resulting emissivities are generally lower by 1% to 2% compared to those obtained in Ref. [22]. Lines strongly affected by collisional transitions exhibit even larger differences; for example, the emissivity of $\lambda 10830$ is 18% lower in the collisionless model. This clearly demonstrates the importance of rigorous treatment of collisional processes in helium atomic models.

From a computational standpoint, implementing a full collisional scheme is challenging, since the number of possible collisional transitions between sublevels in the helium atom increases rapidly with the number of modeled levels: each sublevel is collisionally coupled to all other sublevels.

In our He I emission model we distinguish several types of collisional transitions. Each type of transition is treated by a dedicated method, as described below.

For transitions $\gamma_l \to \gamma_u$ between sublevels with $n \leq 5$, we calculate collisional excitation (transition $l \to u$) and de-excitation (transition $u \to l$) rates using the standard formulas from Ref. [41]:

$$q_{lu} = \frac{8.629 \times 10^{-6}}{\sqrt{T}} \frac{\Upsilon_{ul}(T)}{g_l} \exp\left(-\frac{\Delta E_{ul}}{kT}\right), \tag{27}$$

$$q_{ul} = \frac{8.629 \times 10^{-6}}{\sqrt{T}} \frac{\Upsilon_{ul}(T)}{g_u}. \tag{28}$$

Here, T is temperature in K, g_l and g_u are statistical weights of the corresponding sublevels, and $\Upsilon_{ul}(T)$ is the effective collision strength of the transition. We calculate the effective collision strength using direct integration of collision strength $\Omega(E)$ for the specified temperature T, as follows:

$$\Upsilon_{ul}(T) = \int_0^\infty \Omega(E) \exp\left(-\frac{E}{kT}\right) d\left(\frac{E}{kT}\right). \tag{29}$$

Integration is carried out over an energy grid using the linear interpolation method described in Ref. [42]. The tabulated values of collision strengths as a function of energy E were derived from high-resolution collisional cross section data. The cross section data were computed using the convergent close-coupling method [43,44] and provided by Igor Bray (private communication). This constitutes an important distinction between our helium model and the previous studies. Other independent studies [20–22,45] rely on collisional data from Ref. [25], which is a widely used source of atomic data for collisional transitions between sublevels with $n_l \leq 2$ and $n_u \leq 5$ in the helium atom. In the paper, the authors present extensive tables of thermally averaged collision strengths on a temperature grid. In previous helium atom models, the effective collision strengths were obtained via linear interpolation on this grid, which is relatively sparse in very important range $\sim 10^4 - 2 \times 10^4$ K. Furthermore, for transitions not included in Ref. [25], other studies adopt values from Ref. [19], where a different computational method was used and the data are presented on a different temperature grid. The complementing dataset from Ref. [19] covers transitions between levels up to $n = 4$.

Rather than combining heterogeneous datasets and using the linear interpolation approach applied in earlier works, we integrate the collision strengths directly. This yields a more accurate and internally consistent treatment of collisional transitions between sublevels up to $n = 5$ over the full range of temperatures typical for the interstellar medium of H II regions.

For transitions between sublevels $n_l \leq 5$ and $n_u > 4$, we use scaled collision strengths calculated via the relation from Ref. [46], as follows:

$$\Omega(\gamma_l, \gamma_u, E) = \frac{f_{\gamma_l,\gamma_u}}{f_{\gamma_l,\gamma_5}} \Omega(\gamma_l, \gamma_5, E). \tag{30}$$

Here, $\gamma_5 = [5, l_u, s_u]$. Oscillator strengths are calculated as described in Sec. II B. In case no oscillator strength is available for a transition (this is the case for, e.g., dipole-forbidden transitions), we replace ratio $f_{\gamma_l,\gamma_u}/f_{\gamma_l,\gamma_5}$ with ratio $(5/n_u)^3$, which follows from Born approximation.

For transitions between sublevels with $n_l \geq 5$ and $n_u \geq 5$, the two possible types of transitions are briefly described below. It is important to note that both of these processes are extremely important because they redistribute the populations of Rydberg states toward local thermodynamic equilibrium (LTE).

Transitions occurring between sublevels with the same principal quantum number are called l-changing or Stark collisions. Such collisions modify the orbital angular momentum l of an electron within a fixed principal quantum number n through Stark mixing induced by the electric fields of protons or other heavy charged particles [47,48]. The interaction with the electric field of a heavy particle lifts the energy degeneracy of highly excited sublevels within the n-shell, enabling collisional transitions to take place. Since the energy separation between these sublevels is small, even a low-energy heavy particle can induce a change from one sublevel to another. The slower the particle, the longer the interaction time, and therefore at lower temperatures the probability of transitions induced by heavy particles increases due to the prolonged action of the particle's electric field on the atomic shell. For l-mixing collisions, the main colliders are heavy particles such as protons and ions of He. A great in-depth review of the underlying physics of the process and ways to evaluate the corresponding rates can be found in Refs. [49–51].

Transitions between sublevels with different principal quantum numbers are referred to as n-changing. Since levels with different n are separated by significant energy gaps, only fast-moving electrons can induce collisional transitions between them. A comprehensive review of the underlying physics, along with a comparison of different approximations for collisional rates, is provided in Ref. [52].

We compute the rates of l-changing collisions using the Lmixing package for Python 3 [53]. This package is designed to calculate the rate coefficients for angular momentum mixing of Rydberg atoms in collisions with heavy particles in astrophysical plasmas. In the model, we consider two types of heavy particles: protons and single-ionized helium atoms with number density $n_{He^+} = 0.1 n_p$. Following the recommendations from the authors of the package, we employ the full quantum-mechanical transition probabilities from Refs. [48,54] to evaluate dipole transition rates for levels with $n \leq 30$. For levels with $n > 30$, we adopt the semiclassical approach of Ref. [55]. A limitation of the semiclassical method, however, is that it operates within an unresolved framework and returns only the total collision rate, as follows:

$$q_{nl} = q_{nl,nl+1} + q_{nl,nl-1} \equiv q^+_{nl} + q^-_{nl}. \tag{31}$$

We obtain resolved rates from the unresolved ones using the reciprocity condition from Ref. [51]:

$$q^+_{nl} = \frac{2l+3}{2l+1} q^-_{nl}. \tag{32}$$

Rates are obtained iteratively starting from the sublevel with $l = n-1$, since there is no sublevel with $l = n$ and thus $q^+_{nn-1} = 0$ and $q_{nn-1} = q^-_{nn-1}$.

In addition to the dipole l-changing collisions, we incorporate quadrupole l-changing collisions in our model. The rate of these collisions is calculated using Eq. (C1) from Ref. [56].

We calculate rate of n-changing collisions using straight trajectory Born approximation using the method from Ref. [57] as suggested in Ref. [52]. The rate is calculated via the equation

$$q_{n'n} = \frac{g_n}{g_{n'}} 2\sqrt{\pi} a_0^2 \alpha c n \left[\frac{n'}{Z(n'-n)}\right]^3 \frac{f(\theta)\phi}{\sqrt{\theta}}. \tag{33}$$

Here, g_n and $g_{n'}$ are statistical weights of levels, a_0 is the Bohr radius, and α is the fine structure constant. Variable $\theta = kT/(Z^2 I_H)$, and $f(\theta)$ are given by

$$f(\theta) = \frac{\ln\left(1 + \frac{n\theta}{Z(n'-n)\sqrt{\theta}+2.5}\right)}{\ln\left(1 + \frac{n\sqrt{\theta}}{Z(n'-n)}\right)}. \tag{34}$$

Function ϕ is defined via the following equation:

$$\begin{aligned}\phi = {} & \frac{2n'^2 n^2}{(n'+n)^4 (n'-n)^2} \\ & \times [4(n'-n)-1] \exp\left(\frac{E_n}{kT}\right) E_1\left(\frac{E_n}{kT}\right) \\ & + \frac{8n^3}{(n'+n)^2 (n'-n) n^2 n'^2} \\ & \times (n'-n-0.6)\left(\frac{4}{3} + n^2(n'-n)\right) \\ & \times \left[1 - \left(\frac{E_n}{kT}\right)\exp\left(\frac{E_n}{kT}\right) E_1\left(\frac{E_n}{kT}\right)\right].\end{aligned} \tag{35}$$

Here, E_n is energy of n-level, E_1 is the first exponential integral. The drawback of the rate defined via Eq. (34) is that it returns an unresolved collision rate. To obtain resolved rates, we average over the statistical weight of the initial and final levels as in Ref. [58], as follows:

$$q_{nl,n'l'} = \frac{2l'+1}{n'^2} q_{nn'}. \tag{36}$$

The general algorithm for calculation of collision rates is summarized in the flowchart presented in Fig. 4.

E. Collisional ionization rates

Collisional ionization rates are calculated using the equation

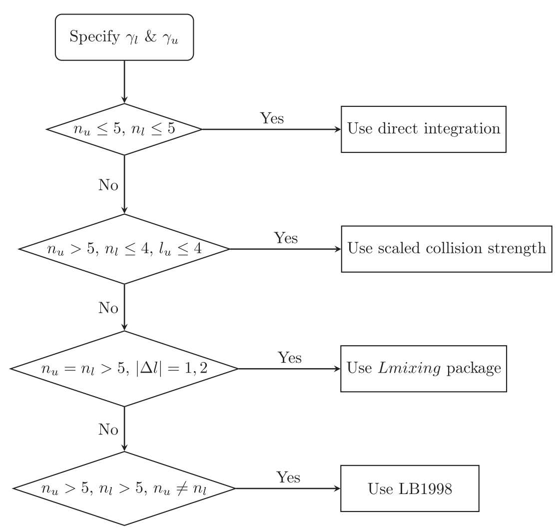

FIG. 4. Flowchart describing the algorithm for calculation of collisional rates in helium atoms. LB1998 corresponds to the collision rate from Ref. [57].

$$C_\gamma^{(ion)}(T) = \sqrt{\frac{8kT}{\pi m_e}} \int_{I_\gamma}^{\infty} \sigma_\gamma^{(ion)}(E) \frac{E}{kT} \exp\left(-\frac{E}{kT}\right) d\frac{E}{kT}. \tag{37}$$

Cross sections for collisional ionization were taken from Ref. [46]. In the paper, the authors provide analytical formulas for the collisional ionization cross sections for levels with $n \leq 4$, which are easily integrable. For levels with $n > 4$, we use the following extrapolation from Ref. [46]:

$$\sigma_{n>4}^{(ion)} = 2.32 \times 10^{-16} \left(\frac{Ry}{E_{n>4}}\right)^2 \left(\frac{x-1}{x^2}\right) \ln(1.25x) \text{ cm}^2. \tag{38}$$

Here, Ry is the Rydberg energy, variable $x = E/E_{n>4}$, and E is the kinetic energy of the colliding electron.

In the model, we do not account for dielectronic recombination, since for the typical physical conditions of H II regions, the rate of this process is 3 to 4 orders of magnitude lower compared to the radiative recombination rate as shown in Ref. [45].

F. Optical depth and photon escape probability

The transition $2^3S \to 1^1S$ is strongly forbidden with $A = 1.27 \times 10^{-4}\ \text{s}^{-1}$ [14]. The 2^3S sublevel is metastable, and an absorption of photons from $n^3P \to 2^3S$ transitions may become quite a significant effect when modeling emissivities of helium lines. This is due to the long lifetime of the 2^3S sublevel, which leads to the emergence of a nonzero optical depth in such lines. We account for radiative transfer effects by replacing A-values for transitions $n^3P \to 2^3S$ with the expression

$$A(n^3P \to 2^3S) \longrightarrow \epsilon(\tau) A(n^3P \to 2^3S). \tag{39}$$

Here, $\epsilon(\tau)$ is the mean photon escape probability and τ is the optical depth in the specified line. We calculate escape probability using the formula from Ref. [13], as follows:

$$\epsilon(\tau) = \frac{1.72}{1.72 + \tau}. \tag{40}$$

Since optical depth in every transition $n^3P \to 2^3S$ is defined by population of metastable 2^3S sublevel, it is convenient to parametrize optical depth of any line in terms of optical depth of some reference line. As a reference line, we use the $\lambda 3889$ line, which corresponds to the transition $3^3P \to 3^3S$ (same as done in Ref. [13]). Optical depth $\tau_{3889} \equiv \tau$ is an additional parameter in the model of helium atoms alongside electron density n_e and temperature T. Optical depths of other lines and the corresponding escape probabilities are calculated using the relation

$$\tau_\lambda = \frac{\lambda^2}{3889^2} \frac{A_\lambda}{A_{3889}} \tau. \tag{41}$$

G. Recombination reminder

If one aims to compute the exact population of a given sublevel in the helium atom (or any other atom), then, strictly speaking, an infinite number of levels would need to be modeled. This is, of course, impossible in practice. Instead, the model must be truncated at some maximum principal quantum number $n_{\max}$, while the contribution of levels with $n > n_{\max}$ must be accounted for separately. Radiative and collisional transitions from such highly excited levels provide an additional and non-negligible channel for populating lower states.

We account for this effect following the approach of Ref. [40]. Specifically, we introduce the recombination reminder α_{rem} as an explicit addition to the direct recombination of the LS-resolved sublevels with $n = n_{\max}$. The recombination reminder is defined as the convergent sum of radiative recombination rates into levels with $n > n_{\max}$. We evaluate α_{rem} using the method of Ref. [59], as follows:

$$\begin{aligned}\alpha_{\text{rem}}(n_{\max}, T) &= \sum_{n=n_{\max}}^{\infty} \alpha_n \\ &= \frac{1}{2} DZ\sqrt{\lambda}\left[\frac{x_{n_{\max}}}{n_{\max}} S_{n_{\max}}(\lambda) + \sigma_{n_{\max}}(\lambda)\right].\end{aligned} \tag{42}$$

Here, $n_{\max}$ is the maximum modeled level, Z is the electric charge, and other quantities are defined via the following equations:

$$\begin{aligned}D &= \frac{64}{3}\sqrt{\frac{\pi}{3}}\alpha^4 c a_0^2 = 5.197 \times 10^{-14}\ \text{cm}^3\ \text{s}^{-1}, \\ \lambda &= \frac{hc\,\text{Ry}\,Z^2}{kT} = 157890 \times \frac{Z^2}{T} \quad \text{where } T \text{ is in K}, \\ x_n &= \frac{\lambda}{n^2}.\end{aligned} \tag{43}$$

Functions S_n and σ_n are determined via the following equations:

$$S_n(\lambda) = \int_0^{\infty} \frac{g_{II}(n, \epsilon)\exp(-x_n u)}{1+u} du, \qquad u = n^2\epsilon, \tag{44}$$

$$\sigma_n(\lambda) = \int_0^{x_n} S_{n'}(\lambda) dx_{n'}. \tag{45}$$

The recombination reminder calculated in this way is then explicitly added to the direct recombination rates of sublevel in $n_{\max}$ level according to their statistical weights, as follows:

$$\alpha(n_{\max}, l, s, T) \longrightarrow \alpha(n_{\max}, l, s, T) + \frac{(2l+1)(2s+1)}{4n_{\max}^2}\alpha_{\mathrm{rem}}(n_{\max}, T). \quad (46)$$

III. MODEL OF HELIUM I EMISSION SPECTRUM

We calculate populations of sublevels in helium atoms as a function of the following parameters: n_e, electron density; T_e, temperature; and τ, optical depth in the $\lambda3889$ line. The general form of the detailed balance equation for population of sublevel γ_k follows the standard form that can be found in, e.g., Ref. [16], as follows:

$$n_e n_{\mathrm{He}} \alpha_k + \sum_{i>k} n_i A_{ik}(\tau) + \sum_X \sum_{j\neq k} n_X n_j q_{jk} = n_k \left[n_e C_k^{(ion)} + \sum_{i<k} A_{ki}(\tau) + \sum_X \sum_{j\neq k} n_X q_{kj} \right]. \quad (47)$$

In this equation, the left-hand part includes all processes that populate sublevel γ_k, and the right-hand part includes all depopulation processes. Population processes include radiative recombination, radiative decay from upper levels relative to γ_k, and collisional transitions of all types from all other levels. Depopulation processes include collisional ionization, radiative decays to lower levels, and again collisional transitions to all other levels from level γ_k. Details on calculation of atomic data are provided in Sec. II. We write down similar equations for every sublevel under consideration and solve the obtained system for sublevel populations using the matrix inversion method.

A cornerstone in constructing such systems of detailed balance equations is the choice of the maximum number of explicitly modeled sublevels. Previous studies adopted different truncation limits, ranging from $n_{\max} = 5$ in Ref. [16] to as many as 40 LS-resolved and 100 n-resolved levels on top of the LS-resolved manifold in Ref. [21]. In this paper, we chose the number of modeled levels according to the methodology proposed in Ref. [58]. The authors provide simple criteria to estimate the maximum number of LS-resolved Rydberg states for which radiative decay rates still dominate over collisional ones. Once collisional processes become faster than radiative decays, the corresponding levels are assumed to be populated according to their statistical weights.

In addition, Ref. [58] investigated the number of explicitly modeled LS-resolved levels required to achieve convergence of the full radiative-recombination cascade. Their results show that, within the relevant range of densities and temperatures, convergence at the $\leq 1\%$ level requires $n_{\max} \gtrsim 25$. To guide the choice of $n_{\max}$, the authors propose the following rule:

$$n_{\max} = n^* + 10, \quad (48)$$

where n^* is the principal quantum number of the level for which the critical electron density n_{crit} equals the model parameter n_e. The critical density is estimated using the empirical relation from Ref. [58]:

$$n_{\mathrm{crit}} = 7.599 \times 10^{13} \cdot n^{-8.675}. \quad (49)$$

We tested the convergence of our model as a function of the number of explicitly modeled sublevels and found good agreement with the results of Ref. [58]. To ensure robustness and avoid potential convergence issues, we adopted a conservative choice of $n_{\max} = 50$, which exceeds the value recommended by the empirical criterion from Ref. [58].

The populations of LS-resolved levels and the emissivities of spectral lines at given values of temperature T, electron density n_e, and optical depth τ are calculated using a dedicated Python 3 code, which we developed especially for this problem. In order to improve performance efficiency of the model, we have precomputed all needed A-values and oscillator strengths for all transitions under consideration and stored them in separate files. Additionally, we have done the same for all energies and effective quantum numbers of LS-resolved sublevels up to specified $n_{\max}$. It allowed us to save about 70% of computational time per a combination of n_e, T, and τ parameters. The total execution time for calculating the sublevel populations was $\sim 150 - 170$ seconds for one set of parameters on an AMD Ryzen 7 8845HS CPU in single thread mode. Testing showed that majority of computational time is spent on calculation of n-changing collisional rates.

IV. RESULTS

A. Emissivities of He I lines

We compute the populations of all LS-resolved sublevels of the helium atom up to $n_{\max} = 50$ using the model described above, for the following grids of electron densities and temperatures. For electron densities, we adopt a linear grid in the range $1 \leq n_e \leq 500$ cm^{-3} with increments of 10 cm^{-3}, and a logarithmic grid with steps of 0.05 dex in the range $500 \leq n_e \leq 1000$ cm^{-3}. For range $1000 \leq n_e \leq 10000$ cm^{-3}, we adopt a logarithmic grid with increments of 0.25 dex. The fine spacing in the low-density range is motivated by observational estimates of electron densities in compact blue dwarf galaxies, which typically fall within $\sim$10–300 cm^{-3}. Modern photoionization models used to infer that helium abundances in H II regions [2,5,6,8–10] employ bilinear interpolation over emissivity grids; hence, a finer density grid improves the accuracy and reliability of the derived observational constraints. For the temperature, we adopt a linear grid spanning $8000 \leq T \leq 22000$ K with increments of 250 K.

TABLE I. Emissivities (10^{-26} erg cm^3 sec^{-1}) of the strongest helium lines, for $n_e = 10^2$ cm^{-3} and $T = 10000$ K. BSS99 stands for Ref. [16], P12 for Ref. [20], and D-Z22 for Ref. [21].

λ	Terms	BSS99	P12	D-Z22	This work
2945	$5^3P - 2^3S$	2.70	2.70	2.70	2.70
3188	$4^3P - 2^3S$	5.62	5.62	5.61	5.62
3889	$3^3P - 2^3S$	13.7	14.0	14.0	14.0
3965	$4^1P - 2^1S$	1.39	1.42	1.41	1.41
4026	$5^3D - 2^3P$	2.86	2.91	2.91	2.92
4388	$5^1D - 2^1P$	0.76	0.77	0.77	0.77
4471	$4^3D - 2^3P$	6.16	6.12	6.13	6.14
4713	$4^3S - 2^3P$	0.65	0.64	0.65	0.65
4922	$4^1D - 2^1P$	1.64	1.65	1.65	1.66
5016	$3^1P - 2^1S$	3.49	3.56	3.55	3.55
5876	$3^3D - 2^3P$	16.9	16.9	17.0	16.9
6678	$3^1D - 2^1P$	4.79	4.80	4.83	4.79
7065	$3^3S - 2^3P$	2.96	2.98	2.98	2.97
7281	$3^1S - 2^1P$	0.90	0.90	0.90	0.90
10830	$2^3P - 2^3S$	34.0	33.4	33.6	33.6
18685	$4^3F - 3^3D$	2.22	2.20	2.23	2.18
20587	$2^1P - 2^1S$	4.13	4.15	4.17	4.16

TABLE II. Emissivities (10^{-26} erg cm^3 sec^{-1}) of the strongest helium lines, for $n_e = 10^2$ cm^{-3} and $T = 20000$ K. BSS99 stands for Ref. [16], P12 for Ref. [20], and D-Z22 for Ref. [21].

λ	Terms	BSS99	P12	D-Z22	This work
2945	$5^3P - 2^3S$	1.68	1.69	1.68	1.69
3188	$4^3P - 2^3S$	3.53	3.50	3.48	3.50
3889	$3^3P - 2^3S$	8.53	8.61	8.59	8.62
3965	$4^1P - 2^1S$	0.81	0.84	0.82	0.83
4026	$5^3D - 2^3P$	1.44	1.48	1.47	1.49
4388	$5^1D - 2^1P$	0.38	0.39	0.38	0.38
4471	$4^3D - 2^3P$	3.11	3.05	3.03	3.05
4713	$4^3S - 2^3P$	0.51	0.49	0.49	0.49
4922	$4^1D - 2^1P$	0.80	0.82	0.80	0.80
5016	$3^1P - 2^1S$	2.01	2.06	2.03	2.04
5876	$3^3D - 2^3P$	8.06	8.13	8.00	7.98
6678	$3^1D - 2^1P$	2.18	2.30	2.18	2.18
7065	$3^3S - 2^3P$	2.22	2.18	2.18	2.18
7281	$3^1S - 2^1P$	0.61	0.61	0.61	0.61
10830	$2^3P - 2^3S$	24.6	23.8	23.6	24.0
18685	$4^3F - 3^3D$	0.92	0.94	0.92	0.90
20587	$2^1P - 2^1S$	2.24	2.29	2.24	2.25

The emissivity of a helium line λ corresponding to a transition from sublevel γ_i to sublevel γ_j is calculated as

$$\frac{4\pi j_\lambda}{n_e n_{\mathrm{He}^+}}(n_e, T) = \frac{n_i(n_e, T)}{n_e n_{\mathrm{He}^+}} A_{ij} E_{ij}. \tag{50}$$

Here $n_i(n_e, T)$ is the population of the upper sublevel γ_i, A_{ij} is the Einstein coefficient for the transition, and E_{ij} is the energy difference between the initial and final sublevels. Thus, the density and temperature dependence of line emissivities is governed by the corresponding dependence of the sublevel populations, which are obtained from the helium atom model at a given values of n_e and T.

We compare our resulting emissivities with the ones presented in literature for a set of so-called "benchmark" lines. This set includes the strongest lines ranging from near-UV to near infrared ranges, and is often used in literature to compare different models of the helium recombination spectrum. The results for $n_e = 100$ cm^{-3}, $T = 10000$ K and $n_e = 100$ cm^{-3}, $T = 20000$ K are presented in Tables I and II. These tables are directly comparable to the Tables 1 and A3 from Ref. [21].

The comparison of emissivities presented in the tables shows excellent agreement between our results and those of previous studies. The average difference with the emissivities reported in Ref. [20] for the majority of lines is ~0.32% at $T = 10000$ K and ~1.16% at $T = 20000$ K, while the corresponding differences with Ref. [21] are ~0.32% and ~0.57%, respectively. The observed discrepancies arise from the use of different atomic datasets for the calculation of collisional rates, as already noted in Sec. II D.

It is important to note that a significant systematic discrepancy was found when comparing the emissivities of the He I λ10830 line with the results of Refs. [20,23]. The emissivity of λ10830 from these papers is systematically underestimated, with the magnitude of the offset growing as the electron density n_e increases. In addition, the tabulated emissivities presented in Ref. [23] (computed using the model from Ref. [20] on a much finer parameter grid) exhibit a visible kink, which becomes more pronounced at higher n_e. These effects are illustrated in Fig. 5.

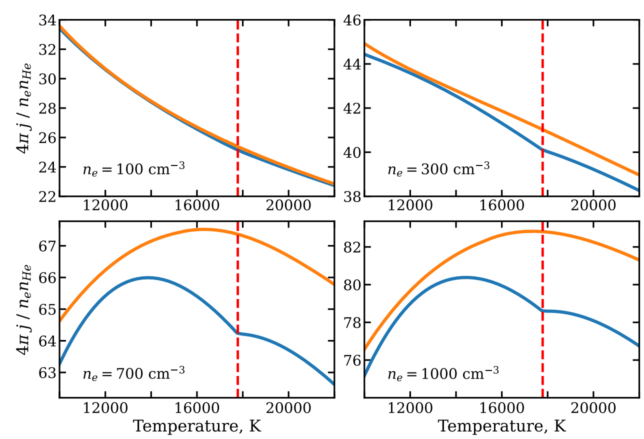

FIG. 5. Emissivities of He I λ10830 line in units 10^{-26} erg cm^3 sec^{-1}, calculated for different electron densities as a function of temperature. Orange lines represent emissivity calculated using our model. Blue lines represent emissivity from Refs. [20,23]. Red dashed lines represent $T = 10^{4.25} = 17783$ K corresponding to the interpolation node on the grid of averaged collision strengths from Ref. [25] (see text).

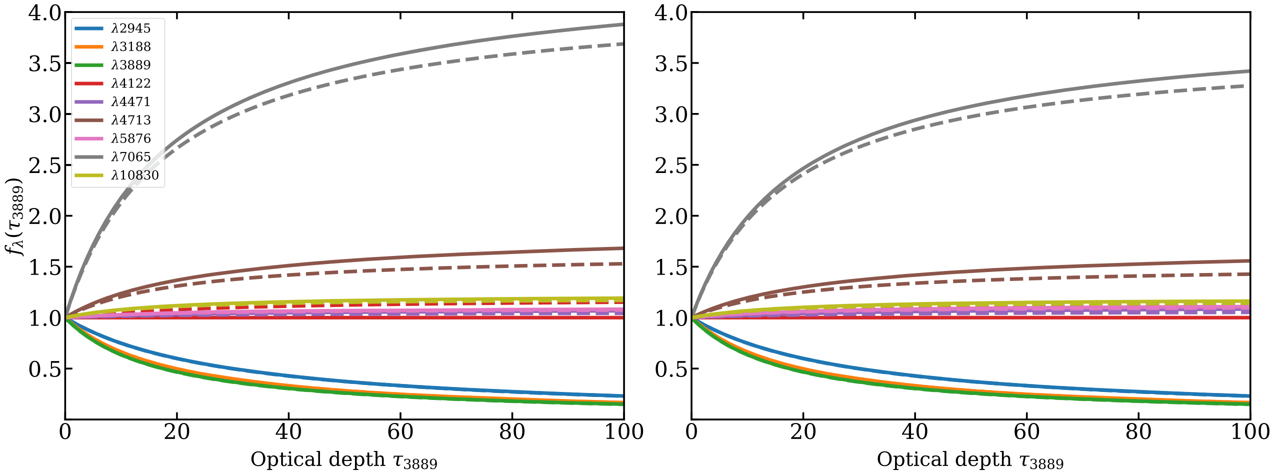

FIG. 6. Optical depth correction function for selected optical lines for cases with electron density $n_e = 100$ cm^{-3} and temperature $T = 10000$ K (left panel) and 20000 K (right panel). Solid lines represent the correction function calculated using our model of He I recombination spectrum, while dashed lines represent results of Ref. [13].

The position of the kink nearly coincides with one of the grid nodes used for linear interpolation of averaged collision strengths from Ref. [25]: the grid node corresponds to $T = 10^{4.25} = 17783$ K, while the kink appears at $T = 17750$ K. At lower densities ($n_e \lesssim 100$ cm^{-3}), the discrepancy between results is not very noticeable. However, as the density increases, so does the discrepancy. This suggests that in the model of Ref. [20] there is a possible issue with the algorithm used to compute collisional rates for transitions involving the 2^3P level, which is the upper level of the transition corresponding to the λ10830 line. Similar problem with λ10830 emissivity from Refs. [20,23] was previously noted and discussed in Ref. [21], where the authors concluded that the differences stem from variations in the treatment of atomic data for collisional rates between low-lying excited levels. Since the λ10830 line is crucial in modern determinations of the primordial ^{4}He abundance—being a key diagnostic of the electron density in galaxies—it must be recognized that the use of emissivity of the λ10830 line from Refs. [20,23] may introduce a systematic bias into the results.

More pronounced deviations are found when comparing our results with those of Ref. [16], where the differences reach ~1%–5% for some lines. This highlights the impact of updated atomic data underlying our model, since all relevant atomic processes included here and in Ref. [16] have been recalculated with newer datasets. This distinction is particularly important, as the present research is focused on radiative transfer corrections for helium lines, while the previously adopted correction function was based on the modified model of Ref. [16]. Accordingly, we may expect similar differences to appear in the optical depth correction function f_τ that would be derived in next subsection.

The complete set of helium emissivities computed over the specified n_e and T grids is too extensive to be published in full, but is available from Zenodo [60].

B. Optical depth correction function

We calculate optical depth correction function using the equation

$$f_\tau(\lambda, n_e, T) = \frac{E_\lambda(\tau \neq 0, n_e, T)}{E_\lambda(\tau = 0, n_e, T)}. \tag{51}$$

The correction function was calculated on the same grid of temperatures and densities as the emissivities. For the optical depth grid, we chose $0 \leq \tau \leq 10$ with 0.5 increments.

We compare our results with the results presented in Ref. [13]. To do that, we fully recreated the model of an He atom described in Refs. [13,16] and repeated the entire cycle of calculations from these papers. We compare our results with those of Ref. [13] in two ways. The first is the general dependence of the correction function on the optical depth for a set of selected helium lines. For this we calculated the correction function for $0 \leq \tau \leq 100$, $n_e = 100$ cm^{-3} and $T = 10000$ K and 20000 K. The dependence of correction functions on optical depth τ for different helium lines is presented on Fig. 6. The figure is directly comparable with Fig. 2 from Ref. [13]. In Fig. 6, results of Ref. [13] are denoted with dashed lines, while our results are denoted with solid ones.

The dependence of the correction functions on optical depth for all lines exhibits a generally similar trend in both models, yet noticeable differences arise and increase with optical depth. For a more quantitative comparison, we plot the relative difference

$$\delta(\lambda, \tau) = \frac{f_{BSS}(\lambda, \tau) - f_{\rm new}(\lambda, \tau)}{f_{BSS}(\lambda, \tau)}. \tag{52}$$

The function $\delta(\lambda, \tau)$ is presented in Fig. 7. The figure shows that the correction functions for lines originating

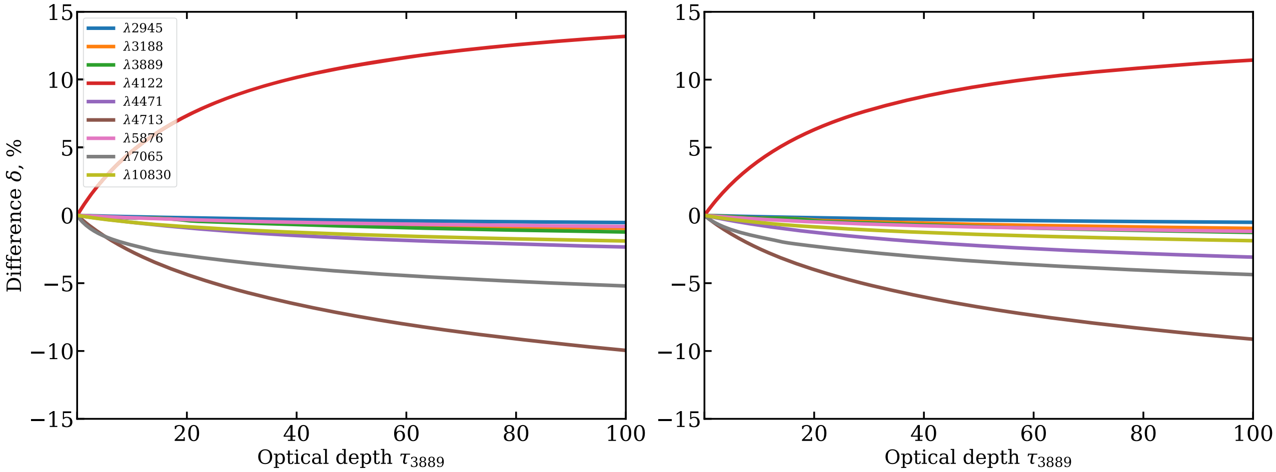

FIG. 7. Relative difference $\delta(\lambda,\tau) = (f_{BSS}(\lambda,\tau) - f_{\rm new}(\lambda,\tau))/f_{BSS}(\lambda,\tau)$ in percent for cases with electron density $n_e = 100$ cm^{-3} and temperature $T = 10000$ K (left panel) and 20000 K (right panel).

from the $n^3P \to 2^3S$ transitions (λ2945, λ3189, λ3889, λ10830) remain essentially identical, with deviations $\leq 1\%$. In contrast, the correction functions for other lines (e.g., λ4122 and λ7065) differ by several percent even in the low optical depth region. This discrepancy is significant in the context of observational data analysis, since line fluxes are typically measured with an accuracy of only a few percent. The observed differences arise because our model is built upon a more advanced and accurate atomic data.

It should also be noted that radiative transfer effects are significant primarily for triplet transitions. For singlet transitions, the influence of the relatively high population of the metastable level is negligible: the deviations of f_τ from unity are $\sim 10^{-3} - 10^{-4}$. These small deviations arise due to collisional mixing between the singlet and triplet ladders. Under the temperatures and densities considered here, this mixing remains weak, which explains the minimal departure from unity.

We compare the theoretical emissivities at a given optical depth, calculated with our model, against values expressed as $E(\lambda, n_e, T) \times f_{BSS}(\lambda, \tau, n_e, T)$. As is customary in all recent studies, the theoretical emissivities $E(\lambda, n_e, T)$ were adopted from Ref. [23] and optical depth function $f_{BSS}(\lambda, \tau, n_e, T)$ is taken from Ref. [13]. The results for $\tau \leq 10$, $n_e = 100$ cm^{-3}, and $T = 10000$ K and 20000 K are shown in Figs. 8 and 9.

Figures 8 and 9 illustrates the deviations between the He I line emissivities obtained in the present study and those predicted by the commonly used approximation $E(\lambda, n_e, T) \times f_{BSS}(\lambda, \tau, n_e, T)$ as a function of optical depth. For most transitions, the discrepancies remain within 1%–2%, but for the λ3889 and λ7065 lines

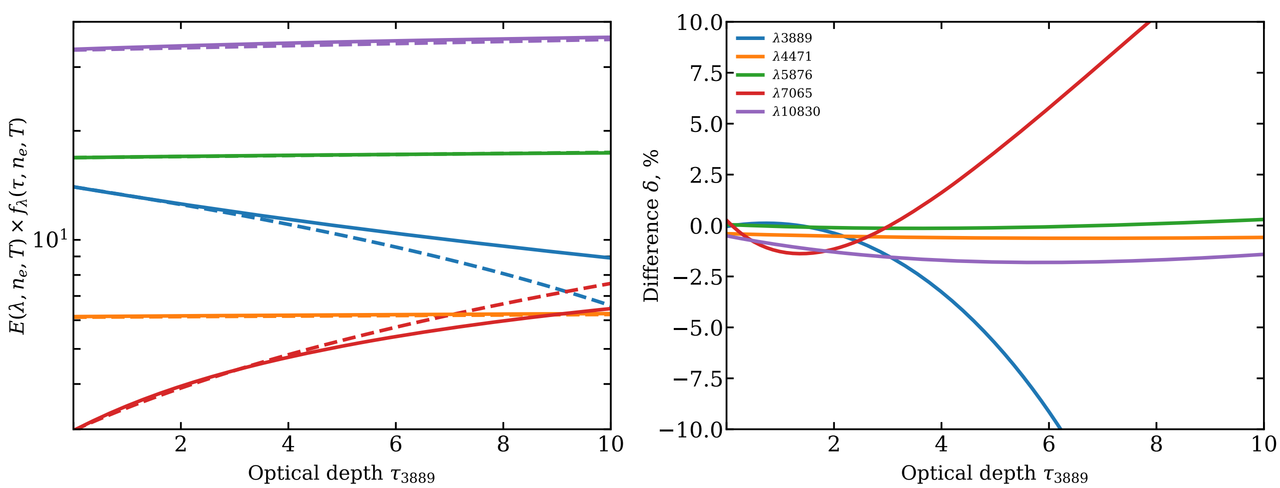

FIG. 8. Emissivities of several He I lines with incorporated radiative transfer corrections as a function of optical depth. Emissivities are calculated for electron density $n_e = 100$ cm^{-3} and temperature $T = 10000$ K. Solid lines represent emissivities calculated using our model He I recombination spectrum. Dashed lines represent product $E(\lambda, n_e, T) \times f_{BSS}(\lambda, \tau, n_e, T)$ based on previous studies (see text). Left panel: absolute values of emissivities in units 10^{26} erg cm^3 sec^{-1}. Right panel: percentage difference between them.

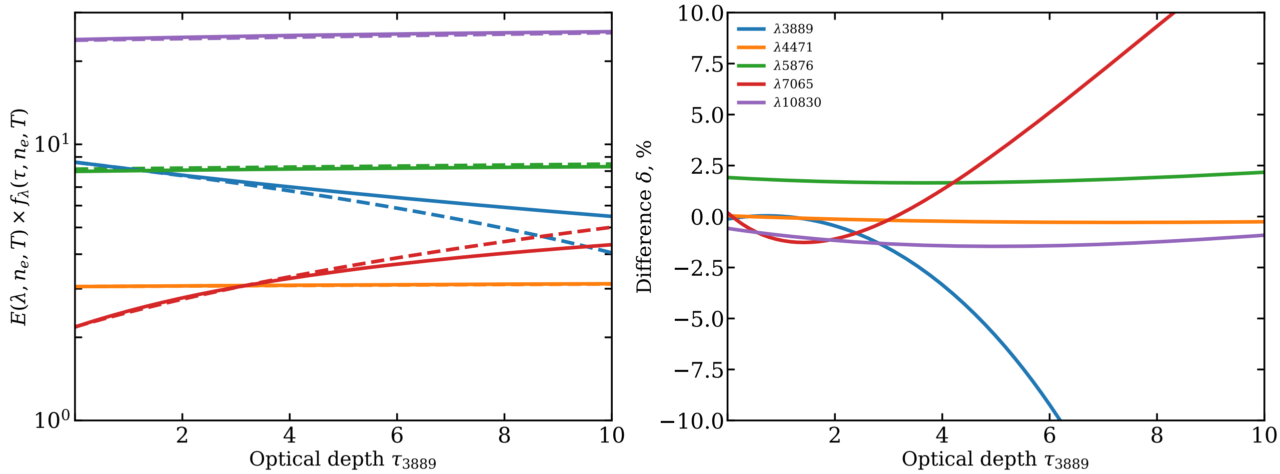

FIG. 9. Same as Fig. 8, but emissivities are calculated for electron density $n_e = 100\ \mathrm{cm}^{-3}$ and temperature $T = 20000$ K.

discrepancies are substantially larger. Specifically, usage of the correction function from Ref. [13] leads to systematic underestimation of the emissivity of $\lambda3889$ (by up to $\sim$20% or more with increasing optical depth) and overestimation of the emissivity of $\lambda7065$ by a comparable amount. Even within the physically realistic range of $\tau \lesssim 5$, the disagreement persists at the 5%–10% level, which is significant for diagnostic applications of these lines.

Such pronounced discrepancies in $\lambda3889$ and $\lambda7065$ arise primarily from the linear dependence on optical depth adopted in correction function from Ref. [13]. Clearly, this dependence is valid only in the limit of small optical depths ($\tau \lesssim 1$), which is not always satisfied in realistic conditions. In addition, the previously discussed 1–2% deviations resulting from the use of more advanced atomic data further contribute to this discrepancy. Taken together, these factors lead to a substantial overall disagreement, which must be carefully considered in future studies and in the analysis of helium emission lines.

C. Approximation of the correction function

For practical use in line diagnostics, calculation of optical depth correction function using full interpolation over the three-dimensional parameter grid of n_e, T, and τ is somewhat inconvenient. This is due to performance issues that arise during the analyses of observational data, since the parameter grids are quite extensive. A reasonable way out in this case is to obtain approximation formulas, similar to the ones from Ref. [13], which would be based on the results of our updated model.

We derive approximation formulas for the following He I lines: $\lambda2945$, $\lambda3188$, $\lambda3889$, $\lambda4026$, $\lambda4471$, $\lambda4713$, $\lambda58760$, $\lambda7065$, and $\lambda10830$. The choice of lines is governed by these lines being the strongest triplet lines of He I in near-UV, visible, and near-IR ranges. As noted previously, for singlet lines, the correction function equals unity with the accuracy of $\sim 10^{-3} - 10^{-4}$. We approximate optical depth correction function $f_\tau(n_e, T)$ using the following relation:

$$f_\tau(n_e, T) = \frac{1 + a(n_e, T) \times \tau}{1 + b \times \tau}. \qquad (53)$$

Here, parameter a is a smooth function of electron density and temperature, and b is constant. This form of approximation function was chosen because (i) it exactly equals to 1 for $\tau = 0$ and (ii) it depends on τ almost linearly in the region $\tau \lesssim 1$, i.e., demonstrates the same behavior as the approximation from Ref. [13], while allowing for smooth nonlinear behavior at higher optical depths.

As shown previously, accounting for radiative transfer may lead to either a decrease or an increase in the emissivities of He I lines. A decrease in emissivity with increasing optical depth is typical for the $n^3P \to 2^3S$ transitions, with the exception of the $\lambda10830$ line corresponding to $2^3P \to 2^3S$. In contrast, other lines from the triplet transition ladder exhibit enhanced emissivity as optical depth grows.

We fit the parameter a as function of the electron density n_e and temperature T using the following relation:

$$a(n_e, T) = \sum_{i=0}^{5} A_i(T) x^i, \qquad x = \lg\left(\frac{n_e}{10^2\ \mathrm{cm}^{-3}}\right). \qquad (54)$$

Here, fit parameters $A_i(T)$ are smooth functions of T defined via the following equation:

$$A_i(T) = \sum_{j=0}^{3} B_i^{(j)} t^j, \qquad t = \lg\left(\frac{T}{10^4 \mathrm{K}}\right). \qquad (55)$$

Overall, the optical depth correction function described by Eq. (53) has 25 fit parameter for each line: b, which

TABLE III. Fitting parameters b and $B_j^{(i)}$ for optical depth correction function defined via Eq. (53) for a set of He I triplet emission lines.

	B_0	B_1	B_2	B_3	B_0	B_1	B_2	B_3
	$\lambda2945$, $b=3.409\times10^{-02}$				$\lambda4713$, $b=4.276\times10^{-02}$			
A_0	4.241×10^{-04}	6.739×10^{-05}	-1.184×10^{-04}	5.959×10^{-05}	7.655×10^{-02}	-1.828×10^{-02}	-1.008×10^{-02}	1.350×10^{-02}
A_1	1.287×10^{-04}	-1.141×10^{-04}	1.408×10^{-05}	-1.418×10^{-06}	-5.368×10^{-04}	-6.202×10^{-03}	-1.149×10^{-02}	2.845×10^{-02}
A_2	-9.949×10^{-05}	1.660×10^{-04}	-9.626×10^{-05}	-7.987×10^{-05}	-9.923×10^{-04}	-7.100×10^{-03}	-1.264×10^{-02}	4.160×10^{-02}
A_3	-6.162×10^{-05}	3.444×10^{-05}	-1.365×10^{-04}	-1.267×10^{-04}	-8.407×10^{-04}	-2.651×10^{-03}	1.107×10^{-02}	-2.577×10^{-03}
A_4	5.217×10^{-05}	-1.052×10^{-04}	-4.027×10^{-05}	6.978×10^{-06}	-6.045×10^{-05}	1.257×10^{-03}	1.165×10^{-02}	-2.130×10^{-02}
A_5	-5.697×10^{-06}	2.270×10^{-05}	2.522×10^{-05}	4.756×10^{-05}	1.820×10^{-04}	3.486×10^{-04}	-5.104×10^{-03}	5.408×10^{-03}
	$\lambda3188$, $b=5.131\times10^{-02}$				$\lambda5876$, $b=4.068\times10^{-02}$			
A_0	6.495×10^{-04}	-5.338×10^{-04}	5.681×10^{-04}	-2.681×10^{-04}	4.507×10^{-02}	3.753×10^{-03}	1.882×10^{-03}	-1.899×10^{-03}
A_1	-6.749×10^{-04}	5.945×10^{-04}	-2.085×10^{-04}	1.430×10^{-05}	-2.264×10^{-04}	-1.975×10^{-04}	-1.024×10^{-03}	-5.707×10^{-03}
A_2	4.537×10^{-04}	-7.174×10^{-04}	5.522×10^{-04}	-2.628×10^{-04}	8.758×10^{-05}	-3.356×10^{-04}	-1.676×10^{-03}	-5.033×10^{-03}
A_3	2.958×10^{-04}	-3.411×10^{-04}	-1.921×10^{-04}	3.284×10^{-04}	9.324×10^{-05}	-3.737×10^{-04}	-1.951×10^{-03}	4.196×10^{-03}
A_4	-2.650×10^{-04}	3.628×10^{-04}	-5.278×10^{-04}	4.049×10^{-04}	-7.755×10^{-05}	-8.592×10^{-05}	-3.971×10^{-04}	4.138×10^{-03}
A_5	3.416×10^{-05}	-5.223×10^{-05}	1.909×10^{-04}	-1.719×10^{-04}	1.304×10^{-05}	8.815×10^{-05}	5.352×10^{-04}	-1.834×10^{-03}
	$\lambda3889$, $b=5.854\times10^{-02}$				$\lambda7065$, $b=5.461\times10^{-02}$			
A_0	7.399×10^{-04}	2.506×10^{-04}	-2.762×10^{-04}	1.422×10^{-04}	2.361×10^{-01}	-8.759×10^{-02}	-5.182×10^{-02}	8.783×10^{-02}
A_1	1.806×10^{-04}	-3.057×10^{-04}	-8.839×10^{-05}	1.853×10^{-04}	-1.132×10^{-02}	-6.569×10^{-02}	-2.734×10^{-02}	1.896×10^{-01}
A_2	-9.546×10^{-05}	1.822×10^{-05}	-3.319×10^{-04}	2.257×10^{-04}	-1.440×10^{-02}	-7.036×10^{-02}	5.927×10^{-02}	1.441×10^{-01}
A_3	-9.595×10^{-05}	-3.434×10^{-05}	-2.756×10^{-04}	4.107×10^{-04}	-6.555×10^{-03}	6.632×10^{-03}	1.216×10^{-01}	-1.965×10^{-01}
A_4	4.975×10^{-05}	-1.233×10^{-04}	2.953×10^{-05}	1.700×10^{-04}	1.941×10^{-03}	3.070×10^{-02}	1.702×10^{-02}	-1.396×10^{-01}
A_5	-2.042×10^{-06}	4.591×10^{-05}	4.476×10^{-05}	-1.138×10^{-04}	9.679×10^{-04}	8.075×10^{-03}	3.082×10^{-02}	7.805×10^{-02}
	$\lambda4026$, $b=-9.988\times10^{-03}$				$\lambda10830$, $b=6.368\times10^{-02}$			
A_0	-9.095×10^{-03}	7.274×10^{-04}	3.047×10^{-04}	-7.155×10^{-05}	7.667×10^{-02}	-5.558×10^{-03}	-6.043×10^{-03}	1.144×10^{-02}
A_1	1.007×10^{-04}	-7.632×10^{-05}	9.027×10^{-05}	-4.993×10^{-04}	-5.435×10^{-03}	-1.455×10^{-02}	1.262×10^{-02}	3.525×10^{-03}
A_2	3.797×10^{-06}	-5.135×10^{-06}	1.064×10^{-04}	-6.808×10^{-04}	-3.630×10^{-03}	1.509×10^{-03}	3.039×10^{-02}	-3.820×10^{-02}
A_3	-3.394×10^{-05}	1.106×10^{-05}	-1.811×10^{-04}	-3.631×10^{-04}	1.018×10^{-03}	7.582×10^{-03}	-8.689×10^{-03}	-3.769×10^{-03}
A_4	1.486×10^{-05}	-2.175×10^{-05}	-1.611×10^{-04}	1.065×10^{-04}	1.281×10^{-03}	-4.800×10^{-04}	-1.722×10^{-02}	2.311×10^{-02}
A_5	-1.713×10^{-06}	4.692×10^{-06}	6.341×10^{-05}	7.705×10^{-05}	-4.396×10^{-04}	-9.710×10^{-04}	6.709×10^{-03}	-6.684×10^{-03}
	$\lambda4471$, $b=2.118\times10^{-03}$							
A_0	4.204×10^{-03}	9.874×10^{-04}	8.248×10^{-04}	-3.394×10^{-04}				
A_1	-5.567×10^{-04}	4.938×10^{-04}	-4.527×10^{-04}	-8.866×10^{-04}				
A_2	4.332×10^{-05}	-4.700×10^{-05}	8.129×10^{-05}	-1.352×10^{-03}				
A_3	1.922×10^{-04}	-2.217×10^{-04}	-6.444×10^{-05}	-4.032×10^{-04}				
A_4	-8.242×10^{-05}	5.455×10^{-05}	-2.957×10^{-04}	4.713×10^{-04}				
A_5	7.268×10^{-06}	5.672×10^{-06}	9.692×10^{-05}	-2.058×10^{-06}				

determines the dependence on optical depth τ, and 24 parameters $B_j^{(i)}$, which govern the temperature and density dependence.

We calculate fit parameters for each line on a three-dimensional grid of n_e, T, and τ using a trust reflective algorithm. Resulting fit parameters are summarized in Table III. The obtained approximation formulas reproduce the directly calculated correction function with an accuracy of $\lesssim 0.1\%$ within the following parameter range: $1 \le n_e \le 10^4$ cm^{-3}, $8000 \le T \le 22000$ K, $0 \le \tau \le 10$.

V. CONCLUSIONS

In this paper, He I line emissivities and the optical depth correction functions for a selected set of the strongest emission lines in the UV, optical, and IR ranges are calculated. The results are obtained using a new collisional-radiative model of the He I recombination spectrum, which is based on modern and accurate atomic data.

The key distinction of the present He I spectrum model, compared to earlier ones, lies in the explicit treatment of nonunity escape probability of photons emerging from transitions to the metastable 2^3S level. Efficient absorption of photons at the metastable level with a non-negligible population leads to a noticeable redistribution of the populations of other levels in the helium atom. Explicit accounting for this effect allows us to incorporate radiative transfer effects directly into the calculated emissivities.

A new set of He I emissivities for the strongest emission lines was calculated for the following electron density and temperature ranges: $1 \leq n_e \leq 10^4$ cm^{-}3 and $8000 \leq T \leq 22000$ K. The calculated emissivities of He I emission lines in the optically thin case show very good agreement with previous studies. Minor deviations ($\lesssim 0.5\%$) are explained by the treatment of collisional rates in earlier models, where linear interpolation over a precomputed grid of thermally averaged collision strengths (restricted to transitions up to $n = 4$) was used. In contrast, in the present work the averaged collision strengths are obtained by direct integration for a larger set of transitions, extending up to $n = 5$.

Using the new model of the He I recombination spectrum, a correction function to account for radiative transfer effects in He I lines is computed. Compared to the function of Ref. [13], obtained with a simplified model, the new function shows systematic deviations of ∼1%–2% within a realistic range of optical depths. These deviations arise from the use of a more advanced model based on modern and more accurate atomic data.

Noticeably larger deviations (up to ∼10% within a realistic parameter range) are found for the product $E(\lambda, n_e, T) \times f_\tau(\lambda, n_e, T)$, which is widely used to describe the emissivity of He I lines at nonzero optical depth. Such significant discrepancies are due to three main reasons:

(1) the new model is based on more recent atomic data and includes a larger number of levels;
(2) the optical-depth function from Ref. [13] relies on a linear dependence on τ, which breaks down for $\tau \gtrsim 1$ for some important lines; and
(3) in current photoionization models, the product $E(\lambda, n_e, T) \times f_\tau(\lambda, n_e, T)$ inadvertently mixes atomic datasets: $E(\lambda, n_e, T)$ is computed with modern atomic data [20], while $f_\tau(\lambda, n_e, T)$ still relies on outdated datasets [13].

To overcome the limited applicability of the function from Ref. [13] and achieve better consistency between the correction function and theoretical He I emissivities, we propose a new fitting function, $f_{\rm new}(\lambda, \tau, n_e, T)$. The function smoothly covers the following ranges of parameters: electron density $1 \leq n_e \leq 10^4$ cm^{-}3, temperature $8000 \leq T \leq 22000$ K, and optical depth $0 \leq \tau \leq 10$. The fitting function has the accuracy of $\lesssim 0.1\%$ within the specified parameter domain.

The obtained results can be easily implemented in all modern studies of the primordial helium abundance as well as in other studies concerned with the analysis of He I emission lines.

ACKNOWLEDGMENTS

This work was supported by the Russian Science Foundation under Grant No. 23-12-00166. O. K. expresses deep gratitude to Dr. Francisco Guzmán for his detailed and valuable explanation of the complexities of the physical picture of collisional transitions in atoms. The authors express a great appreciation to Professors Igor Bray and Yuri Ralchenko for providing the tabulated collision cross sections and valuable advice on the topic.

DATA AVAILABILITY

The data that support the findings of this article are openly available [60].

APPENDIX A: FITTING COEFFICIENTS FOR A-VALUES

This appendix describes fitting coefficients for the oscillator strengths of different transitions of the form $(n, l, s) \longrightarrow (n', l', s)$. The values of quantum numbers for the lower level are denoted with a prime and are considered fixed. The Einstein coefficient for an allowed transition is determined by the formula

$$A_{nl\to n'l'} = \frac{0.667\ \mathrm{cm}^2\ \mathrm{sec}^{-1}}{\lambda^2} \frac{g_{n'l'}}{g_{nl}} f_{nl\to n'l'}. \tag{A1}$$

Oscillator strength is calculated via equation

$$f_{nl\to n'l'} = \frac{1}{\nu^3} \exp\left(ax^2 + bx + c\right). \tag{A2}$$

Here, ν is the effective quantum number of the (n, l, s) level, which is calculated using quantum defects, $x = \ln(E_{n'l's}/\Delta E)$, where $\Delta E = E_{nls} - E_{n'l's}$. Fitting coefficients a, b, c are given in Table IV.

TABLE IV. Fitting coefficients a, b, c used to calculate A-values for dipole allowed transitions in He atoms via the extrapolation of transition data from Ref. [27].

Transition	a	b	c	Transition	a	b	c
$n^1P \to 2^1S$	−0.5212	1.4980	0.8258	$n^3P \to 2^3S$	−1.2552	0.9575	0.3055
$n^1S \to 2^1P$	−0.0667	2.3183	−1.4292	$n^3S \to 2^3P$	−0.0062	2.3165	−1.3656
$n^1D \to 2^1P$	−0.2041	3.1697	1.1341	$n^3D \to 2^3P$	−0.1696	2.8455	1.3102
$n^1P \to 3^1S$	−0.3629	1.6108	1.2713	$n^3P \to 3^3S$	−0.8665	1.2341	0.6799
$n^1S \to 3^1P$	−0.0569	2.3246	−0.3603	$n^3S \to 3^3P$	−0.0115	2.3183	−0.2894
$n^1D \to 3^1P$	−0.2200	2.4906	1.7920	$n^3D \to 3^3P$	−0.2697	2.2448	1.8427
$n^1P \to 3^1D$	−0.3660	2.9286	−2.6734	$n^3P \to 3^3D$	−0.2400	2.7619	−1.9216
$n^1F \to 3^1D$	−0.1381	3.0896	1.2853	$n^3F \to 3^3D$	−0.1943	3.3380	1.4267
$n^1P \to 4^1S$	−0.3006	1.7246	1.6071	$n^3P \to 4^3S$	−0.7341	1.4638	0.9610
$n^1S \to 4^1P$	−0.0467	2.3228	0.3040	$n^3S \to 4^3P$	−0.0078	2.3139	0.3696
$n^1D \to 4^1P$	−0.1468	2.2748	2.1984	$n^3D \to 4^3P$	−0.1985	2.0782	2.1801
$n^1P \to 4^1D$	−0.2738	2.7738	−1.4383	$n^3P \to 4^3D$	−0.1814	2.6539	−0.7813
$n^1F \to 4^1D$	−0.2268	2.5973	1.9472	$n^3F \to 4^3D$	−0.2575	2.7239	2.0930
$n^1D \to 4^1F$	−0.3916	3.3412	−3.3231	$n^3D \to 4^3F$	−0.3843	3.3271	−2.9957
$n^1G \to 4^1F$	−0.2711	3.7808	1.5045	$n^3G \to 4^3F$	−0.2721	3.7828	1.5314
$n^1P \to 5^1S$	−0.2758	1.8294	1.8733	$n^3P \to 5^3S$	−0.6850	1.6723	1.1762
$n^1S \to 5^1P$	−0.0408	2.3223	0.7859	$n^3S \to 5^3P$	−0.0054	2.3102	0.8460
$n^1D \to 5^1P$	−0.1065	2.1902	2.5024	$n^3D \to 5^3P$	−0.1575	2.0307	2.4379
$n^1P \to 5^1D$	−0.2243	2.6910	−0.6640	$n^3P \to 5^3D$	−0.1469	2.5900	−0.0655
$n^1F \to 5^1D$	−0.1675	2.3629	2.3354	$n^3F \to 5^3D$	−0.1887	2.4414	2.4813
$n^1D \to 5^1F$	−0.3040	3.1131	−1.9805	$n^3D \to 5^3F$	−0.3021	3.1079	−1.7250
$n^1G \to 5^1F$	−0.3177	3.1087	2.2473	$n^3G \to 5^3F$	−0.3182	3.1100	2.2861
$n^1F \to 5^1G$	−0.4604	3.8089	−3.4727	$n^3F \to 5^3G$	0.0	2.9204	−3.0172
$n^1H \to 5^1G$	−0.3193	4.1129	1.4451	$n^3H \to 5^3G$	−0.3180	4.1104	1.4591
$n^1P \to 6^1S$	−0.2647	1.9245	2.0906	$n^3P \to 6^3S$	−0.6805	1.8866	1.3347
$n^1S \to 6^1P$	−0.0359	2.3203	1.1646	$n^3S \to 6^3P$	−0.0014	2.3024	1.2210
$n^1D \to 6^1P$	−0.0887	2.1630	2.7455	$n^3D \to 6^3P$	−0.1439	2.0427	2.6420
$n^1P \to 6^1D$	−0.1928	2.6388	−0.1011	$n^3P \to 6^3D$	−0.1262	2.5514	0.4557
$n^1F \to 6^1D$	−0.1287	2.2530	2.6123	$n^3F \to 6^3D$	−0.1398	2.2988	2.7609
$n^1D \to 6^1F$	−0.2540	2.9795	−1.1413	$n^3D \to 6^3F$	−0.2505	2.9720	−0.9195
$n^1G \to 6^1F$	−0.2374	2.7265	2.6690	$n^3G \to 6^3F$	−0.2382	2.7281	2.7173
$n^1F \to 6^1G$	−0.3637	3.4985	−2.1657	$n^3F \to 6^3G$	−0.3553	3.4705	−2.0873
$n^1H \to 6^1G$	−0.3608	3.4253	2.3087	$n^3H \to 6^3G$	−0.3609	3.4253	2.3218
$n^1G \to 6^1H$	−0.4846	4.1284	−3.8739	$n^3G \to 6^3H$	−0.4846	4.1384	−3.8739
$n^1I \to 6^1H$	−0.3591	4.4223	1.2858	$n^3I \to 6^3H$	−0.3607	4.4249	1.2940
$n^1P \to 7^1S$	−0.2675	2.0248	2.2657	$n^3P \to 7^3S$	−0.7162	2.1488	1.4243
$n^1S \to 7^1P$	−0.0359	2.3203	1.1646	$n^3S \to 7^3P$	0.0007	2.2974	1.5292
$n^1D \to 7^1P$	−0.0765	2.1523	2.9516	$n^3D \to 7^3P$	0.0	1.7561	2.9838
$n^1P \to 7^1D$	−0.1745	2.6098	0.3368	$n^3P \to 7^3D$	−0.1105	2.5211	0.8670
$n^1F \to 7^1D$	−0.1002	2.1876	2.8356	$n^3F \to 7^3D$	−0.1111	2.2258	2.9811
$n^1D \to 7^1F$	−0.2189	2.8875	−0.5330	$n^3D \to 7^3F$	0.0	2.3661	−0.0380
$n^1G \to 7^1F$	−0.1744	2.5022	2.9645	$n^3G \to 7^3F$	−0.1744	2.5023	3.0202
$n^1F \to 7^1G$	−0.2992	3.2931	−1.3247	$n^3F \to 7^3G$	−0.2958	3.2783	−1.2494
$n^1H \to 7^1G$	−0.2744	2.9744	2.8118	$n^3H \to 7^3G$	−0.2722	2.9693	2.8277
$n^1G \to 7^1H$	−0.3931	3.7817	−2.5038	$n^3G \to 7^3H$	0.0	2.8458	−1.9605
$n^1I \to 7^1H$	−0.3976	3.7215	2.2533	$n^3I \to 7^3H$	−0.3976	3.7215	2.2533
$n^1H \to 7^1I$	−0.5194	4.4687	−4.3716	$n^3H \to 7^3I$	−0.5194	4.4749	−4.3716

APPENDIX B: FITTING COEFFICIENTS FOR SCALING FACTOR

Fitting coefficients for scaling factor $f(T,\gamma)$, which is used to calculate radiative recombination rate to sublevel $\gamma = [n,l,s]$, are as follows:

$$\alpha_\gamma(T) = f(T,\gamma) \times \alpha_{\mathrm{H}}(T,n,l). \tag{B1}$$

Scaling factor $f(T,\gamma)$ is defined via the following equation:

$$f(T,\gamma) = \frac{a_1(T)}{n^{a_2(T)}} + a_3(T). \tag{B2}$$

Here, $a_i(T)$ are fit coefficients. Their dependence on temperature is determined by a fourth-degree polynomial with temperature T in K with fitting coefficients $b_j^{(i)}$ being presented in Table V, as follows:

$$a_i(T) = \sum_{j=0}^{4} b_j^{(i)} \left(\frac{T}{10^4\ \mathrm{K}}\right)^j. \tag{B3}$$

TABLE V. Fitting coefficients used to calculate scaling term for radiative recombination rate to sublevels in He atoms with $l \leq 2$ and $s = 1, 3$.

	b_4	b_3	b_2	b_1	b_0
$l=0,\ s=1$					
a_1	3.84×10^{-03}	-2.75×10^{-02}	7.72×10^{-02}	-9.76×10^{-02}	1.72×10^{-01}
a_2	1.34×10^{-02}	-9.85×10^{-02}	2.89×10^{-01}	-4.09×10^{-01}	$1.24\times10^{+00}$
a_3	-6.69×10^{-04}	5.34×10^{-03}	-1.86×10^{-02}	4.71×10^{-02}	1.28×10^{-01}
$l=0,\ s=3$					
a_1	1.62×10^{-02}	-1.16×10^{-01}	3.21×10^{-01}	-3.53×10^{-01}	6.98×10^{-01}
a_2	1.65×10^{-02}	-1.22×10^{-01}	3.56×10^{-01}	-4.96×10^{-01}	$1.36\times10^{+00}$
a_3	-1.98×10^{-03}	1.60×10^{-02}	-5.67×10^{-02}	1.56×10^{-01}	1.89×10^{-01}
$l=1,\ s=1$					
a_1	-1.95×10^{-03}	1.30×10^{-02}	-3.48×10^{-02}	4.73×10^{-02}	-9.39×10^{-02}
a_2	8.52×10^{-03}	-4.67×10^{-02}	8.96×10^{-02}	-5.46×10^{-02}	$1.26\times10^{+00}$
a_3	2.69×10^{-04}	-2.13×10^{-03}	6.96×10^{-03}	-1.38×10^{-02}	2.77×10^{-01}
$l=1,\ s=3$					
a_1	3.36×10^{-03}	-2.87×10^{-02}	9.56×10^{-02}	-1.48×10^{-01}	5.49×10^{-01}
a_2	-1.95×10^{-04}	-5.29×10^{-03}	3.62×10^{-02}	-8.47×10^{-02}	$1.16\times10^{+00}$
a_3	-1.65×10^{-03}	1.32×10^{-02}	-4.62×10^{-02}	1.18×10^{-01}	7.41×10^{-01}
$l=2,\ s=1$					
a_1	1.49×10^{-03}	-9.16×10^{-03}	2.17×10^{-02}	-2.57×10^{-02}	2.57×10^{-02}
a_2	8.49×10^{-02}	-4.94×10^{-01}	$1.07\times10^{+00}$	$-1.03\times10^{+00}$	$1.47\times10^{+00}$
a_3	1.99×10^{-05}	-1.26×10^{-05}	-4.23×10^{-04}	1.44×10^{-03}	2.47×10^{-01}
$l=2,\ s=3$					
a_1	2.30×10^{-03}	-1.24×10^{-02}	2.40×10^{-02}	-2.12×10^{-02}	-4.22×10^{-02}
a_2	-6.50×10^{-02}	4.08×10^{-01}	$-1.00\times10^{+00}$	$1.30\times10^{+00}$	2.49×10^{-01}
a_3	8.27×10^{-04}	-5.62×10^{-03}	1.47×10^{-02}	-1.72×10^{-02}	7.99×10^{-01}

[1] Y. I. Izotov, T. X. Thuan, and N. G. Guseva, A new determination of the primordial He abundance using the He I λ10830 Å emission line: Cosmological implications, Mon. Not. R. Astron. Soc. **445**, 778 (2014).

[2] E. Aver, K. A. Olive, and E. D. Skillman, The effects of He I λ10830 on helium abundance determinations, J. Cosmol. Astropart. Phys. 07 (2015) 011.

[3] M. Valerdi, A. Peimbert, M. Peimbert, and A. Sixtos, Determination of the primordial helium abundance based on NGC 346, an H II region of the small magellanic cloud, Astrophys. J. **876**, 98 (2019).

[4] V. Fernández, E. Terlevich, A. I. Díaz, and R. Terlevich, A Bayesian direct method implementation to fit emission line spectra: Application to the primordial He abundance determination, Mon. Not. R. Astron. Soc. **487**, 3221 (2019).

[5] O. A. Kurichin, P. A. Kislitsyn, V. V. Klimenko, S. A. Balashev, and A. V. Ivanchik, A new determination of the primordial helium abundance using the analyses of H II region spectra from SDSS, Mon. Not. R. Astron. Soc. **502**, 3045 (2021).

[6] T. Hsyu, R. J. Cooke, J. X. Prochaska, and M. Bolte, The PHLEK survey: A new determination of the primordial helium abundance, Astrophys. J. **896**, 77 (2020).

[7] M. Valerdi, A. Peimbert, and M. Peimbert, Chemical abundances in seven metal-poor H II regions and a determination of the primordial helium abundance, Mon. Not. R. Astron. Soc. **505**, 3624 (2021).

[8] E. Aver, D. A. Berg, K. A. Olive, R. W. Pogge, J. J. Salzer, and E. D. Skillman, Improving helium abundance determinations with Leo P as a case study, J. Cosmol. Astropart. Phys. 03 (2021) 027.

[9] E. Aver, D. A. Berg, A. S. Hirschauer, K. A. Olive, R. W. Pogge, N. S. J. Rogers, J. J. Salzer, and E. D. Skillman, A comprehensive chemical abundance analysis of the extremely metal poor Leoncino Dwarf galaxy (AGC 198691), Mon. Not. R. Astron. Soc. **510**, 373 (2022).

[10] O. A. Kurichin, P. A. Kislitsyn, and A. V. Ivanchik, Determination of H II region metallicity in the context of estimating the primordial helium abundance, Astron. Lett. **47**, 674 (2021).

[11] A. Matsumoto *et al.*, EMPRESS. VIII. A new determination of primordial He abundance with extremely metal-poor galaxies: A suggestion of the lepton asymmetry and implications for the Hubble tension, Astrophys. J. **941**, 167 (2022).

[12] H. Yanagisawa *et al.*, EMPRESS. XV. A new determination of the primordial helium abundance suggesting a moderately low Y_P value, arXiv:2506.24050.

[13] R. A. Benjamin, E. D. Skillman, and D. P. Smits, Radiative transfer effects in He I emission lines, Astrophys. J. **569**, 288 (2002).

[14] G. Łach and K. Pachucki, Forbidden transitions in the helium atom, Phys. Rev. A **64**, 042510 (2001).

[15] He I λ3889 line (transition $3^3P \to 2^3S$) is used for normalization since it is the strongest line with a finite opacity in visible range. The closest alternatives to λ3889 such as λ3188 and λ10830 fall in the UV and IR ranges, respectively, and therefore are less suitable for the analysis and modeling of optical spectra.

[16] R. A. Benjamin, E. D. Skillman, and D. P. Smits, Improving predictions for helium emission lines, Astrophys. J. **514**, 307 (1999).

[17] D. P. Smits, Low-temperature recombination coefficients and nova-shell abundances., Mon. Not. R. Astron. Soc. **248**, 193 (1991).

[18] D. P. Smits, Theoretical HeI line intensities in low-density plasmas, Mon. Not. R. Astron. Soc. **278**, 683 (1996).

[19] P. Sawey and K. Berrington, Collision strengths from a 29-state r-matrix calculation on electron excitation in helium, At. Data Nucl. Data Tables **55**, 81 (1993).

[20] R. L. Porter, G. J. Ferland, P. J. Storey, and M. J. Detisch, Improved He I emissivities in the case B approximation, Mon. Not. R. Astron. Soc. **425**, L28 (2012).

[21] G. Del Zanna and P. J. Storey, Helium line emissivities for nebular astrophysics, Mon. Not. R. Astron. Soc. **513**, 1198 (2022).

[22] R. L. Porter, R. P. Bauman, G. J. Ferland, and K. B. MacAdam, Theoretical He I emissivities in the Case B approximation, Astrophys. J. **622**, L73 (2005).

[23] E. Aver, K. A. Olive, R. L. Porter, and E. D. Skillman, The primordial helium abundance from updated emissivities, J. Cosmol. Astropart. Phys. 11 (2013) 017.

[24] D. A. Berg, R. L. Sanders, A. E. Shapley, M. W. Topping, N. A. Reddy, E. D. Skillman, E. Aver, F. Cullen, C. T. Donnan, J. S. Dunlop, T. Jones, A. A. Khostovan, D. J. McLeod, D. Narayanan, P. A. Oesch, A. J. Pahl, M. Pettini, N. M. Förster Schreiber, and D. P. Stark, The AURORA Survey: Robust helium abundances at high redshift reveal a subpopulation of helium-enhanced galaxies in the early universe, arXiv:2507.17057.

[25] I. Bray, A. Burgess, D. V. Fursa, and J. A. Tully, $\mathrm{He}(1^1\mathrm{S}, 2^3\mathrm{S}, 2^1\mathrm{S}, 2^3\mathrm{P} \to \mathrm{n}^{1,3}L)$: Thermally averaged electron collision strengths for n $n <= 5$, Astron. Astrophys. Suppl. Ser. **146**, 481 (2000).

[26] S. Navas *et al.* (Particle Data Group), Review of particle physics, Phys. Rev. D **110**, 030001 (2024).

[27] G. W. F. Drake and D. C. Morton, A multiplet table for neutral helium (^{4}He I) with transition rates, Astrophys. J. Suppl. Ser. **170**, 251 (2007).

[28] G. W. F. Drake, *Springer Handbook of Atomic, Molecular, and Optical Physics* (Springer, New York, 2006).

[29] G. W. F. Drake and R. A. Swainson, Quantum defects and the 1/n dependence of Rydberg energies: Second-order polarization effects, Phys. Rev. A **44**, 5448 (1991).

[30] D. G. Hummer and P. J. Storey, Recombination of helium-like ions—I. Photoionization cross-sections and total recombination and cooling coefficients for atomic helium, Mon. Not. R. Astron. Soc. **297**, 1073 (1998).

[31] D. R. Bates and A. Damgaard, The calculation of the absolute strengths of spectral lines, Phil. Trans. R. Soc. A **242**, 101 (1949).

[32] J. Hey, On forms of the coulomb approximation as a useful source of atomic data for the spectroscopy of astrophysical and fusion plasmas, J. Phys. B **50**, 065701 (2017).

[33] S. Klarsfeld, Alternative forms of the Coulomb approximation for bound-bound multipole transitions, Phys. Rev. A **39**, 2324 (1989).

[34] H. Regemorter, H. Dy, and M. Prud'homme, Radial transition integrals involving low or high effective quantum

numbers in the coulomb approximation, J. Phys. B **12**, 1053 (2001).
[35] I. I. Sobelman, *Atomic Spectra and Radiative Transitions* (Springer, New York, 1979).
[36] D. A. Varshalovich, A. N. Moskalev, and V. K. Khersonskii, *Quantum Theory of Angular Momentum* (World Scientific, Singapore, 1988).
[37] B. T. Draine, *Physics of the Interstellar and Intergalactic Medium* (Princeton University Press, Princeton, NJ, 2011).
[38] P. Storey and D. Hummer, Fast computer evaluation of radiative properties of hydrogenic systems, Comput. Phys. Commun. **66**, 129 (1991).
[39] G. W. F. Drake, Spontaneous two-photon decay rates in hydrogenlike and heliumlike ions, Phys. Rev. A **34**, 2871 (1986).
[40] R. P. Bauman, R. L. Porter, G. J. Ferland, and K. B. MacAdam, J-resolved He I emission predictions in the low-density limit, Astrophys. J. **628**, 541 (2005).
[41] D. E. Osterbrock and G. J. Ferland, *Astrophysics of Gaseous Nebulae and Active Galactic Nuclei* (University Science Books, Sausalito, CA, 2006).
[42] A. Burgess and J. A. Tully, On the analysis of collision strengths and rate coefficients, Astron. Astrophys. **254**, 436 (1992).
[43] I. Bray, Convergent close-coupling method for the calculation of electron scattering on hydrogenlike targets, Phys. Rev. A **49**, 1066 (1994).
[44] D. V. Fursa and I. Bray, Calculation of electron-helium scattering, Phys. Rev. A **52**, 1279 (1995).
[45] G. Del Zanna, P. J. Storey, N. R. Badnell, and V. Andretta, Helium line emissivities in the solar corona, Astrophys. J. **898**, 72 (2020).
[46] Y. Ralchenko, R. K. Janev, T. Kato, D. V. Fursa, I. Bray, and F. J. de Heer, Electron-impact excitation and ionization cross sections for ground state and excited helium atoms, At. Data Nucl. Data Tables **94**, 603 (2008).
[47] R. M. Pengelly and M. J. Seaton, Recombination spectra, II, Mon. Not. R. Astron. Soc. **127**, 165 (1964).
[48] D. Vrinceanu and M. R. Flannery, Classical and quantal collisional stark mixing at ultralow energies, Phys. Rev. A **63**, 032701 (2001).
[49] F. Guzmán, N. R. Badnell, R. J. R. Williams, P. A. M. van Hoof, M. Chatzikos, and G. J. Ferland, H, He-like recombination spectra—I. l-changing collisions for hydrogen, Mon. Not. R. Astron. Soc. **459**, 3498 (2016).
[50] F. Guzmán, N. R. Badnell, R. J. R. Williams, P. A. M. van Hoof, M. Chatzikos, and G. J. Ferland, H-, He-like recombination spectra—II. l-changing collisions for He Rydberg states, Mon. Not. R. Astron. Soc. **464**, 312 (2017).
[51] N. R. Badnell, F. Guzmán, S. Brodie, R. J. R. Williams, P. A. M. van Hoof, M. Chatzikos, and G. J. Ferland, H, He-like recombination spectra—IV. Clarification and refinement of methodology for l-changing collisions, Mon. Not. R. Astron. Soc. **507**, 2922 (2021).
[52] F. Guzmán, M. Chatzikos, P. A. M. van Hoof, D. S. Balser, M. Dehghanian, N. R. Badnell, and G. J. Ferland, H-, He-like recombination spectra—III. n-changing collisions in highly excited Rydberg states and their impact on the radio, IR, and optical recombination lines, Mon. Not. R. Astron. Soc. **486**, 1003 (2019).
[53] D. Vrinceanu, R. Onofrio, J. B. R. Oonk, P. Salas, and H. R. Sadeghpour, Efficient computation of collisional ℓ-mixing rate coefficients in astrophysical plasmas, Astrophys. J. **879**, 115 (2019).
[54] D. Vrinceanu, R. Onofrio, and H. R. Sadeghpour, Angular momentum changing transitions in proton-Rydberg hydrogen atom collisions, Astrophys. J. **747**, 56 (2012).
[55] D. Vrinceanu, R. Onofrio, and H. R. Sadeghpour, On the treatment of ℓ-changing proton-hydrogen Rydberg atom collisions, Mon. Not. R. Astron. Soc. **471**, 3051 (2017).
[56] E. Deliporanidou, N. R. Badnell, P. J. Storey, G. Del Zanna, and G. J. Ferland, H, He-like recombination spectra VI: Quadrupole l-changing collisions, Mon. Not. R. Astron. Soc. **539**, 2957 (2025).
[57] V. S. Lebedev and I. L. Beigman, *Physics of Highly Excited Atoms and Ions* (Springer, Berlin, Heidelberg, 1998), Vol. 22.
[58] F. Guzmán, M. Chatzikos, and G. J. Ferland, H-, He-like recombination spectra—V. On the dependence of the simulated line intensities on the number of electronic levels of the atoms, Mon. Not. R. Astron. Soc. **539**, 2939 (2025).
[59] M. J. Seaton, Radiative recombination of hydrogenic ions, Mon. Not. R. Astron. Soc. **119**, 81 (1959).
[60] O. A. Kurichin and A. V. Ivanchik, He I emissivity table, Zenodo Repository (2025), https://zenodo.org/records/17195751.